Department of Civil, Geo and Environmental Engineering
Chair of Hydromechanics

Validation of RANS Turbulence Models for Subsonic Turbulent Boundary Layer Flows Under Families of Pressure Gradients

Yasunari Nishi

Master's Thesis

submitted in fulfilment of the requirements for the Master's degree in Computational Mechanics

Matriculation number: 03722549

Supervisor: Prof. Dr.-Ing. habil. Michael Manhart, TU München

Advisors: Dr. Tobias Knopp, DLR

Philip Ströer, DLR

Dr. Andreas Krumbein, DLR

Date of submission: January 19, 2022

Delcaration of Authorship

With this statement, I declare that I have independently completed this Master's thesis. The thoughts taken directly or indirectly from external sources are properly marked as such. This thesis was not previously submitted to another academic institution and has also not yet been published.

Yasunari Nishi

Munich, January 19, 2022

The present work was developed in collaboration with German Aerospace Center (DLR) in Göttingen, Germany.

Abstract

The present thesis aims to provide a validation database of existing RANS models for high Reynolds number flows with history effects due to streamwise changing mild pressure gradients, and to assess the predictive accuracy and its uncertainty of each RANS model. For this purpose, two recent wind tunnel experiments with mild pressure gradients were selected, and the two-dimensional computational set-ups for RANS simulations were defined. The first test case is the Virginia Tech wind tunnel experiment conducted in the framework of the North Atlantic Treaty Organization (NATO) Science & Technology Organization (STO) Air Vehicles Technology (AVT) 349 project (Fritsch et al. (2022)). The second test case considered is the Laboratoire de Mécanique de Lille (LML) wind tunnel experiment by Cuvier et al. (2017). Both flow cases encompass streamwise changing mild pressure gradients, which result in the non-equilibrium effects and history effects. For both test cases, the influence of changes in the computational setup and their sensitivities were investigated. The RANS simulations were carried out using three turbulence models, the SA-neg, the Menter SST, and the SSG/LRR-ω models and the results were compared with the experimental data.

The experimental and RANS results are in good agreement in regions where the flow is in near equilibrium. Some appreciable discrepancies are observed in the region where the flow is at APG and in non-equilibrium. However, the deviations are relatively small due to mild pressure gradients, which is a further reason to demand highly accurate measurement data. The largest deviations of the RANS predictions from the experimental data are found in the regions of the largest non-equilibrium, i.e., in the regions of the largest streamwise changes in the local pressure gradient. Also, the greater discrepancy is observed in the LML test case than the Virginia Tech test case, which is most likely due to the larger pressure gradient coefficient. These observations might suggest that the existing RANS models, that are calibrated for equilibrium boundary layer flows, fail to capture all details of non-equilibrium effects. Comparisons of different RANS models reveal a fairly less model dependency on both test cases than might be expected. This could be explained by the fact that the SSG/LRR-ω model uses the same length-scale equation (i.e., $\omega-$equation) as the Menter SST model, and all models are mainly calibrated for equilibrium turbulent boundary layer flows. Also, comparisons of different numerical set-ups demonstrate the difficulty of reproducing a 3D experimental set-up in 2D computations.

Acknowledgments

Firstly, I am deeply grateful to my supervisor at DLR Göttingen, $C^2A^2S^2E^2$ department, Dr. Tobias Knopp, for guiding me throughout the project. Regular discussions with him have tremendously helped me to improve my understanding of turbulent flows and their CFD simulations. His arguments and explanations on my results always made the direction of this research clear. I would not be able to complete this work without his continuous and great support.

I would also like to thank a colleague of mine at DLR, Philip Ströer, for his support, especially at the beginning of the project. Thanks to his guidance, I was able to get used to software such as DLR TAU-code, Tecplot, and Pointwise very quickly and proceed with my work efficiently. In addition, I would like to thank the head of $C^2A^2S^2E^2$ department Dr. Cornelia Grabe and our team leader Dr. Andreas Krumbein for accepting me as a Master thesis student and giving me the opportunity to work as a member of this great Turbulence and Transition team. I have learned a lot from inspiring discussions in the meetings or seminars, and it has expanded my research interests.

Besides my DLR colleagues, I appreciate Prof. Michael Manhart for accepting this topic and his supervision from the side of TU München.

I would also like to express my gratitude to the collaborators from the North Atlantic Treaty Organization (NATO) Science & Technology Organization (STO) Air Vehicles Technology (AVT) 349 Research Technology Group (RTG). There have been many fruitful discussions during which we were preparing for the SciTech 2022 paper. Especially, I acknowledge Daniel J. Fritsch from Virginia Tech for organizing this collaboration and regular discussions. Also, I would like to thank all who contributed to the Virginia Tech wind tunnel experiment measurements for their great effort and for providing us with precious data.

Regarding the LML wind tunnel experiment that is described in the present work, I would like to thank Dr. Christophe Cuvier from the University of Lille Nord de France for providing us with additional data and further information on the experiment. Also, I acknowledge Dr. Christian Willert from DLR Köln, who contributed to these experimental measurements, for his support on this test case.

Without financial support, my whole study in Germany would not be possible. I would like to show my gratitude to the Shigeta Education Foundation in Japan for providing the scholarship during my Master's study.

I must express my gratitude to my family for always being supportive of what I want to do, their continuous financial support, encouragement, and love. I understand that everything would be easier if I had stayed in Japan. But they supported my decision and let me explore a different side of the

world. I promise that I will give back to them as much as I can in the future. And I sincerely thank all my family members for being such a great family. Also, I would like to thank my girlfriend for her continuous support, encouragement, and understanding. I appreciate her for making my life colorful and making me always stay positive. Lastly, I would like to thank all my friends for helping, inspiring, sharing, and always bringing laughter. This achievement would not be possible without them.

Contents

Abstract **IV**

Acknowledgements **VI**

Table of Contents **VIII**

List of Figures **XI**

List of Tables **1**

1 Introduction **2**
1.1 Motivation 2
1.2 Objectives 4
1.3 Organization of Thesis 4

2 Literature Review **5**
2.1 Turbulent Boundary Layer Flows at Pressure Gradients 5
2.1.1 Turbulent Boundary Layers at Zero Pressure Gradient 5
2.1.2 Turbulence Boundary Layers at Pressure Gradients 6
2.2 Validation of RANS Models for TBL Flows at Pressure Gradients 9

3 Numerical Methodology: The DLR-TAU code **10**
3.1 Governing Equations 10
3.1.1 Compressible Navier-Stokes Equations 10
3.1.2 Compressible Reynolds-Averaged Navier-Stokes Equations 11
3.2 Turbulence Models 12
3.2.1 Treatments of the Reynolds Stress Tensor 12
3.2.2 The Spalart-Allmaras One Equation Model 13
3.2.3 Two-Equation k-ω Shear Stress Transport (SST) Model 15
3.2.4 SSG/LRR-ω Reynolds Stress Model 18
3.3 Discretizaiton Scheme 19
3.3.1 Discretization of Computational Domain 19
3.3.2 Spatial Discretization 20
3.3.3 Time Discretization 21

4 The Virginia Tech Stability Wind Tunnel Experiment **23**
4.1 Experimental set-ups . . . 23
4.1.1 Flow Case . . . 23
4.1.2 Measurement Techniques . . . 24
4.1.3 Reference Point . . . 25
4.2 Computational set-ups . . . 25
4.2.1 Computational Grids . . . 25
4.2.2 Numerical Methods . . . 26
4.3 Results . . . 28
4.3.1 Boundary layer parameters . . . 29
4.3.2 Wall profiles . . . 37
4.4 Summary . . . 42

5 LML Wind Tunnel Experiment **43**
5.1 Experimental set-ups . . . 43
5.1.1 Description of the Experiment . . . 43
5.1.2 Measurement Technique . . . 45
5.2 Computational set-ups . . . 48
5.2.1 Computational Grid . . . 48
5.2.2 Numerical Methods . . . 49
5.2.3 Different numerical set-ups and modification of the top wall . . . 49
5.3 Results . . . 51
5.3.1 Boundary Layer Parameters . . . 51
5.3.2 Wall Profiles . . . 57
5.4 Summary . . . 66

6 Conclusions **67**
6.1 Conclusions . . . 67
6.2 Recommendations for Future Work . . . 71

Bibliography **77**

List of Figures

2.1 Viscous scaled mean velocity profiles of the adverse pressure gradient flows by Nagano et al. (1993). P^+ in the legend denotes Δp_s^+ previously shown. The increment of the wake part can be observed. 8

2.2 Viscous scaled mean velocity profiles of the favorable pressure gradient flows by Jones et al. (2001). In contrast to the adverse pressure gradient flows by Nagano et al. (1993), the wake part was suppressed. 8

2.3 Correlation between defect shape factor G and pressure gradient parameter β from Skåre and åge Krogstad (1994). The dashed curve represents the curve by Mellor and Gibson (1966), and the black dot represents the experimental data by Skåre and åge Krogstad (1994). 8

3.1 Exemplary hybrid primary grid (black) and the corresponding dual grid (red) around a NACA-0021 airfoil (Reuß (2015)) 20

4.1 Flow case set-up 24

4.2 A rake of Pitot tubes mounted on the port-side wall (bottom wall in Fig. 4.1). 25

4.3 Flow case set-up 26

4.4 Computational Grid for 12° (Level 5) 26

4.5 Pressure and skin coefficients computed for the 12° case using SA-neg for five different grid levels. 27

4.6 Pressure and skin coefficients computed for the 12° case. The three vertical dashed lines in (a) represent the three rake measurement stations (P3, P5, and P7) where wall profiles are studied in the present work. 30

4.7 Different boundary layer thicknesses and the shape factor computed for the 12° case. The experimental results show the rake measurement data at P3 to P9. 31

4.8 Distribution of Rotta-Clauser parameter β and defect shape factor G vs. β computed for the 12° case. The experimental results show the rake measurement data at P3 to P9. 33

4.9 Pressure and skin coefficients computed for the −10° case. The three vertical dashed lines in (a) represent the three rake measurement stations (P3, P5, and P7) where wall profiles are studied in the present work. 34

4.10 Different boundary layer thicknesses and the shape factor computed for the −10° case. The experimental results show the rake measurement data at P3 to P9. 35

4.11 Distribution of Rotta-Clauser parameter β and defect shape factor G vs. β computed for the −10° case. The experimental results show the rake measurement data at P3 to P9. 36

4.12 The viscous scaled mean velocity profiles at three stations (P3, P5, and P7) computed for the 12° case. Log-law with $\kappa = 0.41, B = 5.0$ and linear relation in the viscous sublayer are marked with black dashed lines. The experimental results show the rake measurement data. 38
4.13 The mean velocity profiles U/U_e vs. y/δ_{95} at three stations (P3, P5 and P7) computed for the 12° case. The experimental results show the rake measurement data. 39
4.14 The mean velocity profiles U/U_e vs. y/δ_{95} at three stations (P3, P5 and P7) computed for the −10° case. Log-law with $\kappa = 0.41, B = 5.0$ and linear relation in the viscous sublayer are marked with black dashed lines. The experimental results show the rake measurement data. 40
4.15 The mean velocity profiles U/U_e vs. y/δ_{95} at three stations (P3, P5 and P7) computed for the −10° case. The experimental results show the rake measurement data. 41

5.1 The LML boundary layer wind tunnel with the ramp model (Cuvier et al. (2017)) . . 44
5.2 The CAD geometry of the ramp model (Cuvier et al. (2017)) 44
5.3 The illustration of the ramp geometry (Cuvier et al. (2017)) 44
5.4 The global and local coordinate systems. The global coordinate x starts at the test section entrance, and y at the bottom wall. The curvilinear coordinate s starts from the leading edge of the ramp model and is along the surface of the ramp. 45
5.5 The sketch of the experimental set-ups and PIV measurement positions. The marks in red represent the stations which will be considered in the following Results section. . . 45
5.6 The developed hybrid computational grid. 48
5.7 Sketch of the concept of top wall geometry modification proposed by Vaquero et al. (2019). 50
5.8 Modified top wall geometry obtained using the SA-neg turbulence model. 51
5.9 Pressure coefficient C_p on the top and bottom wall obtained with set-up No. 1. 52
5.10 Different boundary layer thicknesses and the shape factor computed with set-up No. 1. 53
5.11 Skin friction coefficient and the edge velocity obtained with set-up No. 1. 54
5.12 Comparison of the edge velocity between the three different set-ups. 54
5.13 Comparison of pressure coefficients C_p on the top and bottom wall between the three different set-ups. 55
5.14 Comparison of boundary layer parameters between the three different set-ups. 56
5.15 The stations considered in the present work. The stations (i), (ii), (iii), and (iv) in the FPG region are located at $s = 1362\,\text{mm}$, $s = 2392\,\text{mm}$, $s = 3050\,\text{mm}$, and $s = 3497\,\text{mm}$ respectively. The stations (1), (2), and (3) in the APG region are located at $s = 3983\,\text{mm}$, $s = 5233\,\text{mm}$, and $s = 5858\,\text{mm}$ respectively. 57
5.16 The mean velocity and TKE profiles in wall unit at the inflow ZPG reference station. The results are obtained by computational set-up No. 1. Log-law with $\kappa = 0.41, B = 5.0$ and linear relation in the viscous sublayer are marked with black dashed lines. 58
5.17 The mean velocity profiles in wall unit at three stations in the APG region. The results are obtained by computational set-up No. 1. Log-law with $\kappa = 0.41, B = 5.0$ and linear relation in the viscous sublayer are marked with black dashed lines. 60
5.18 The Reynolds stress profiles in wall unit at three stations in the APG region. The results are obtained by the computational set-up No. 1. 61

5.19 Dimensional mean velocity profiles at four stations in the FPG region. The results are obtained by the computational set-up No. 2 using the SA-neg. 62
5.20 Dimensional mean velocity profiles at three stations in the APG region. The results are obtained by the computational set-up No. 2 using the SA-neg. 63
5.21 The mean velocity profiles in wall unit obtained with three different set-ups at the ZPG reference station and two stations in the APG region. The results are acquired by using the SA-neg model. Log-law with $\kappa = 0.41, B = 5.0$ and linear relation in the viscous sublayer are marked with black dashed lines. 64
5.22 The mean velocity profiles in dimensional unit obtained with three different set-ups at the ZPG reference station and two stations in the APG region. The results are acquired by using the SA-neg model. 65

List of Tables

3.1 Closure coefficients of Menter SST model in TAU 18

4.1 Rake probe measurement positions in the steramwise direction 24
4.2 Grid metrics of the 2D grid family 27
4.3 Reference conditions 28

5.1 Baseline reference conditions. 49
5.2 Three different numerical set-ups considered in the present work. 50

Chapter 1

Introduction

1.1 Motivation

Computational Fluid Dynamics (CFD) is an essential tool to understand the flow phenomena that occur in many engineering problems. Due to the growth of available computational resources, the role of CFD in industries has been becoming more and more important. In fluid dynamics, the complexity of the flow is governed by the Reynolds number. The higher the Reynolds number is, the more complex features the flow has. At low Reynolds numbers, the flow is laminar, i.e., fluid particles smoothly travel in layers. At high Reynolds numbers, the flow becomes turbulent, i.e., fluid particles travel chaotically and irregularly. In many practical fluid dynamic problems such as the flow over a wing of aircraft, the flow is turbulent rather than laminar. However, the turbulence is essentially three-dimensional, multi-scale, unsteady, random, and chaotic motions, and this fact makes it challenging to replicate turbulence flows in computers correctly.

The most straightforward but most expensive method to tackle this challenge is Direct Numerical Simulation (DNS). In DNS, one directly applies the Navier-Stokes equations and tries to resolve all the turbulence scales from the Kolmogorov scale to the largest flow pattern without any models. However, this requires a significant number of grid points, and the computational cost increases as the Reynolds number goes up because the ratio of the largest eddy to the smallest is proportional to $\propto Re^{3/4}$. In three-dimensional computations, the computational cost increases by the factor of $Re^{9/4}$. For this reason, even with a state-of-the-art supercomputer, the DNS is still not applicable to high Reynolds number turbulent flows, which are of great interest in many industrial applications. The Large Eddy Simulation (LES) is another approach, where large scale eddies are directly resolved, but small scale eddies are modeled by filtering of the original Navier-Stokes equations. Due to the less computational cost than DNS and its capability to capture the turbulence behaviors, the LES has been extensively used as a tool to understand the unknown physics of turbulence flows, and such simulations in the literature play an important role as a database of turbulence flows. However, the LES still requires a large computational resource, and it has not yet been used as a standard numerical tool in the industry.

For the above-mentioned reasons, the Reynolds-Averaged-Navier-Stokes (RANS) simulation has been used as a standard tool in the industry for the last decades due to its affordable cost and its applicability to high Reynolds number flows. In RANS simulations, one solves the statistically averaged Navier-Stokes equations with modeling and the resulting new unknown term — Reynolds stress term. Since the Prandtl's mixing length idea (Prandtl (1925)), different modeling approaches and their variants have been proposed, modified, and calibrated — Baldwin and Lomax model (Baldwin and Lomax (1978)), $k - \epsilon$ model (Jones and Launder (1972)), $k - \omega$ model (Wilcox (1988)), Spalart-Allmaras (SA) model (Spalart and Allmaras (1992)), $k - \omega$ SST (Menter (1994)), and the list continues. In the aerospace field, especially the SA model, the Menter SST model, and their variants have been most commonly used and have proved their capabilities of predicting many relevant turbulent flows.

Despite those successes in RANS turbulence modelings history, there are still open questions on their performances and predictive accuracy for complex real-world flows. One such example is a turbulent boundary layer flow with pressure gradients, which is of the main interest in the present work. Pressure gradients can influence the development of the boundary layers (e.g., the thickness of the boundary layer or profiles of mean velocity and turbulence quantities) and potentially result in separation. For example, an adverse pressure gradient decelerates the flow, which could lead to the separation eventually, while a favorable pressure gradient stabilizes the boundary layer and reduce the turbulence. Although we have several understandings of the effects of pressure gradients, unfortunately, we are still far away from the full knowledge of such flows. For example, the effects of pressure gradients on the mean velocity profiles are still under debate, e.g., the existence of log-law and half-power-law (sqrt-law) (Perry et al. (1966); Knopp et al. (2021)). When the flow is subjected to streamwise changing pressure gradients, the boundary layer could be non-equilibrium (not self-preserving) and contain the history effects (Mellor and Gibson (1966); Bobke et al. (2017)). How to characterize and quantify such effects are also still open in the literature. Due to the limited understanding of pressure gradient effects, the commonly used existing RANS models do not incorporate such effects as a modeling term or a coefficient explicitly but have mainly been calibrated for simple canonical flows such as turbulent boundary layers at zero pressure gradient (ZPG). Therefore, their predictive accuracy for pressure gradient flows is questionable, and modeling improvement for these flows is of great interest.

For this purpose, establishing well-defined validation test cases is a crucial task, which turbulence modelers can use for the validation and/or calibration of their RANS models for pressure gradient flows. However, such validations are still rare in the literature due to the lack of carefully designed experiments that are intended to be used as CFD test cases. It should be worth mentioning that such validation test cases for high Reynolds number flows can only be achieved based on wind tunnel experiments since the DNS approach is not applicable in this regime. To tackle this problem, in the present study, two recent wind tunnel experiments with pressure gradients have been selected, and efforts to set them up as validation test cases have been made. The first test case is the wind tunnel experiment conducted in the Virginia Tech Stability Wind Tunnel (see Fritsch et al. (2020)) in the framework of the North Atlantic Treaty Organization (NATO) Science & Technology Organization (STO) Air Vehicles Technology (AVT) 349 project on "Non-Equilibrium Turbulent Boundary Layers in High Reynolds Number Flow at Incompressible Conditions". This flow case involves streamwise changing mild pressure gradients and hence is expected to contain non-equilibrium effects. The second test case is the wind tunnel experiment conducted in the Laboratoire de Mécanique de Lille (LML) wind tunnel (Cuvier et al. (2017)) in the framework of the EuHIT European project (`www.euhit.org`). This flow case has approximately constant pressure gradient regions but slightly stronger pressure

gradients. Both experiments have been designed such that modelers can use them as CFD test cases, and therefore they are suitable for this purpose.

1.2 Objectives

The objectives of the present work are summarized as follows:

- To provide a validation database of existing RANS models for high Reynolds number flows with history effects due to streamwise changing mild pressure gradients
- To assess the predictive accuracy and its uncertainty of RANS models for the established validation test cases

1.3 Organization of Thesis

In Chapter 2, theoretical backgrounds and known phenomena on turbulent boundary layer flows subjected to pressure gradients will be described. In Chapter 3, the numerical methodology used in the present work will be described, including discretization methods and turbulence models. In Chapter 4, the first test case, the Virgina Tech wind tunnel experiment, will be discussed. Description of the experimental and numerical setup will be given, and finally, the obtained results will be discussed. In Chapter 5, another test case, the LML wind tunnel experiment, will be described, and corresponding results will be discussed. Finally, Chapter 6 will present the conclusions of the main results and suggestions for future work.

Chapter 2

Literature Review

This chapter provides a literature review of previous research on turbulence boundary layer flows at pressure gradients. Firstly, some of the important experimental and theoretical studies will be reviewed. Subsequently, previous research on validations of the existing RANS models with experimental results will be described.

2.1 Turbulent Boundary Layer Flows at Pressure Gradients

2.1.1 Turbulent Boundary Layers at Zero Pressure Gradient

For turbulent boundary layers at zero pressure gradient (ZPG), for sufficiently large Reynolds numbers, the existence of the universal logarithmic law in the mean velocity profile has been demonstrated by a large number of experiments and is widely accepted.

$$u^+ = \frac{1}{\kappa} \log\left(y^+\right) + B, \tag{2.1}$$

where

$$u^+ = \frac{u}{u_\tau}, \quad y^+ = \frac{y u_\tau}{\nu}, \tag{2.2}$$

with u being the mean velocity, $u_\tau = \sqrt{\tau_w/\rho}$ the friction velocity, τ_w the wall shear stress, ρ the freestream density, y the wall distance, ν the kinematic viscosity, κ the von Kármán constant, and B the intercept. The intercept B is known to be dependent on the wall roughness. Different values for κ and B are reported in the literature. The most classical ones are $\kappa = 0.41$ and $B = 5.0$ by Coles and Hirst (1969), while $\kappa = 0.384$ and $B = 4.17$ were found by Österlund et al. (2000). See also Marusic et al. (2013) for an overview.

The turbulent boundary layer at ZPG is typically divided into four layers: the viscous sublayer ($y^+ < 5$), the buffer layer ($5 < y^+ < 30$), the logarithmic layer ($30 < y^+ < 0.15\,\delta^+$), and the wake layer ($y^+ > 0.15\,\delta^+$), with δ being the boundary layer thickness. The first three layers (i.e., the

viscous sublayer, the buffer layer, and the logarithmic layer) are often collectively called an inner region, while the logarithmic layer and the wake layer are called an outer region. Note that different studies reported slightly different values from each other for the bounds of the logarithmic layer.

In contrast to the turbulent boundary layer flows at ZPG, a universal wall law for the inner region for the turbulent boundary layers at pressure gradients, particularly at adverse pressure gradients, has not been found until now. For the APG TBL flows, the region between the buffer and wake layers is often called the overlap layer. The structure of the overlap layer and its universality remain open in the literature.

2.1.2 Turbulence Boundary Layers at Pressure Gradients

Experimental and theoretical study

The foundation of the turbulent boundary layer flows at pressure gradients was made by Clauser Clauser (1954, 1956) over 50 years ago. He defined a non-dimensional pressure gradient parameter, which has been commonly used in the literature. The pressure gradient parameter β (sometimes called Rottta-Clauser pressure gradient parameter) is defined as Eq. (2.3), where δ^* being displacement thickness, ρ the density, u_τ the friction velocity, P the pressure, and s the streamwise coordinate. He claimed that a boundary layer flow departs from equilibrium when β is not constant.

$$\beta_{RC} = \frac{\delta^*}{\rho u_\tau^2} \frac{\partial P}{\partial s} \tag{2.3}$$

The term "equilibrium" in regards to the turbulent boundary layer flows seems to be often confused by the community. The strict definition of the equilibrium boundary layer is proposed by Townsend (1956) and later by Rotta (1962). According to their definition, all mean-relative motions and energy-containing components of turbulence (e.g., Reynolds shear stress and the turbulence intensities) have to be invariant with the streamwise position when scaled with local velocity and length scales (see also Marusic et al. (2010)). Rotta showed that this condition can only be satisfied by the sink-flow boundary layer on a smooth wall. Later, the sink flow experiment by Jones et al. (2001) validated this theory at high Reynolds numbers ($1800 < Re_\theta < 3000$). Following this strict definition, turbulent boundary layer flows at zero pressure gradient are not in equilibrium but near-equilibrium.

Around the same time as Clauser (1956), Coles (1956) proposed to represent the mean velocity profile with a linear combination of two universal laws: the law-of-the-wall and law-of-the-wake (Eq. (2.4)), which includes pressure gradient effects. In Eq. (2.4), Π is the Coles wake factor, W_c is the Coles wake function, δ is the boundary layer thickness.

$$u^+ = \frac{1}{\kappa} \log(y^+) + B + \frac{\Pi}{\kappa} W_c \left[\frac{y}{\delta}, \Pi\right] \tag{2.4}$$

As mentioned earlier, the overlap layer's structure and its universality are still open. Various propositions have been made in the literature. One of them is the two-layer structure hypothesis that the overlap layer is divided into two layers. This hypothesis originates from Stratford (1959), who proposed a square-root law (also referred to as sqrt-law or half-power law) for the velocity profile in his

analysis using a velocity scale based on the pressure gradient u_p. The definition of u_p is shown in Eq. (2.5). This velocity scale was considered as more appropriate than a friction velocity u_τ in the case of APG because in the extreme APG case, the flow will separate, and u_τ becomes zero.

$$u_p \equiv \left(\frac{\nu}{\rho}\frac{dP}{ds}\right)^{1/3} \tag{2.5}$$

Stratford's sqrt-law was later extended by Townsend (1961) who used u_τ as a velocity scale and obtained a law with a logarithmic part and a square-root part. Afzal (1996) arrived at similar expressions to Townsend using asymptotic matching (Eq. (2.6)).

$$u^+ = \frac{1}{\kappa}\left[\log\left(y^+\right) + 2\left(\sqrt{1+\Delta p_s^+ y^+} - 1\right) + 2\log\left(\frac{2}{\sqrt{1+\Delta p_s^+ y^+}+1}\right)\right] + B, \tag{2.6}$$

where Δp_s^+ denotes

$$\Delta p_s^+ = \frac{\nu}{\rho u_\tau^3}\frac{\partial P}{\partial s}. \tag{2.7}$$

Another hypothesis, the three-layer structure was also studied by Yajnik (1970), Mellor and Gibson (1966), and later Durbin and Belcher (1992). They are all based on asymptotic analysis.

Regarding the non-equilibrium effects of the turbulent boundary layers, Mellor and Gibson (1966) postulated that there is a universal relations between the defect shape factor $G = (1 - 1/H)/(u_\tau/U_e)$ and the pressure coefficient parameter β, where $H = \delta^*/\theta$ being the shape factor, δ^* the displacement thickness, θ the momentum thickness, u_τ the friction velocity, and U_e the edge velocity.

One of the important classical experiments was conducted by Nagano et al. (1993), who studied turbulent boundary layer flows with moderate to strong adverse pressure gradients ($\beta_{RC} = 0.76-4.66$). They found that the mean velocity profile in viscous scaling shifts downwards from the standard logarithmic law with an increasing adverse pressure gradient, suggesting a reduction in the sub-layer thickness. The same observations were later reported by other studies, including Monty et al. (2011). In contrast, Dixit and Ramesh (2010) among others found the shift-up of the mean velocity profile for strong FPG flows. In Nagano et al. (1993), it was also observed that the wake part pushes up as the magnitude of the adverse pressure gradient increases (see Fig. 2.1). The opposite trend was observed in several FPG flow experiments, i.e., the wake part shifts down due to the FPG (see Fig. 2.2).

Skåre and åge Krogstad (1994) investigated an equilibrium boundary layer flows with a strong adverse pressure gradient ($\beta_{RC} = 12.2 - 21.4$). They analyzed the turbulent kinetic energy (TKE) budgets and found that the pressure gradient does not affect the distribution mechanism of the TKE for their equilibrium boundary layer flows. Fig. 2.3 shows the comparison of their experimental data with the relations for the equilibrium TBLs proposed by Mellor and Gibson (1966).

Some of the more recent experiments for the pressure gradient flows are e.g., Anderson (2011), Harun (2012), Volino (2020), and Knopp et al. (2021). Harun (2012) gives a good review of known and unknown pressure gradient effects.

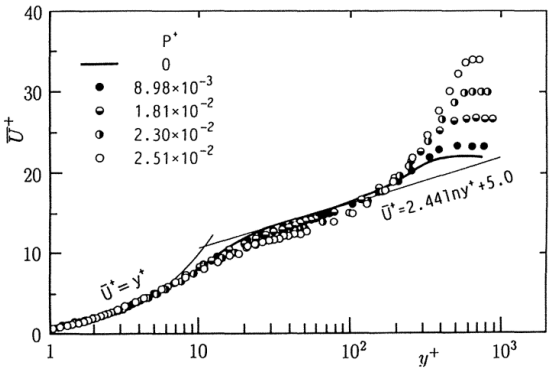

Fig. 2.1: Viscous scaled mean velocity profiles of the adverse pressure gradient flows by Nagano et al. (1993). P^+ in the legend denotes Δp_s^+ previously shown. The increment of the wake part can be observed.

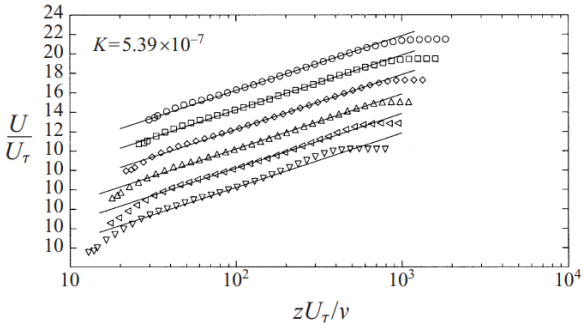

Fig. 2.2: Viscous scaled mean velocity profiles of the favorable pressure gradient flows by Jones et al. (2001). In contrast to the adverse pressure gradient flows by Nagano et al. (1993), the wake part was suppressed.

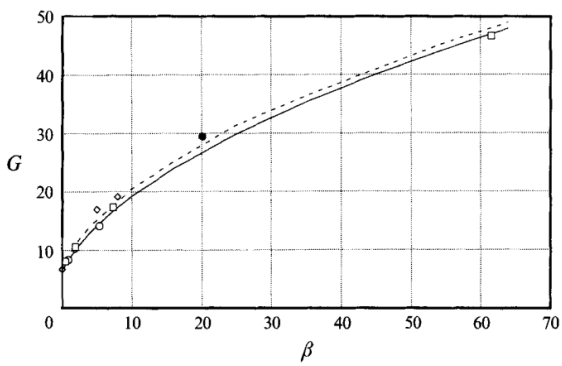

Fig. 2.3: Correlation between defect shape factor G and pressure gradient parameter β from Skåre and åge Krogstad (1994). The dashed curve represents the curve by Mellor and Gibson (1966), and the black dot represents the experimental data by Skåre and åge Krogstad (1994).

Numerical study

In addition to the experimental studies, numerical studies have also been conducted thanks to the progress of the computational power. Some of the earliest DNS simulations of turbulent boundary layer flows at pressure gradients are found in Spalart and Leonard (1987); Spalart and Watmuff (1993). Later, Lee and Sung (2009) investigated equilibrium adverse pressure gradient flows using DNS simulations. More recently, adverse pressure gradient flows containing small separation bubbles were studied using DNS simulations by Coleman et al. (2018).

Apart from DNS simulations, near-equilibrium boundary layers under adverse pressure gradients were studied by Bobke et al. (2017) using Large Eddy Simulations (LES). They focused on the history effects in the adverse pressure gradients and found that Clauser pressure-gradient parameter and the Reynolds number are not sufficient to characterize the flow states.

2.2 Validation of RANS Models for TBL Flows at Pressure Gradients

As mentioned in Chapter 1, establishing well-defined validation test cases for pressure gradient flows at high Reynolds numbers is an important task for calibrations and/or improvements of the existing RANS modes for pressure gradient flows. Despite its demands, such validation test cases are still rare.

One of the recent attempts is found in Knopp et al. (2022), where a turbulent boundary layer flow subjected to a strong adverse pressure gradient was experimentally and numerically investigated. Modifications of the existing RANS models were also attempted earlier by Knopp (2016), where the modification of $k-\omega$ type models incorporating a sqrt-law for the mean velocity profile were considered, which is a similar idea by Rao and Hassan (1998). This work was later extended for SSG/LRR-ω model in Knopp (2019).

Vaquero et al. (2019) considered the experimental work by Cuvier et al. (2017) and compared different simulation techniques including RANS, hybrid RANS/LES, and Zonal Detached Eddy Simulation (ZDES). They observed that the mean velocity profiles in the APG region were poorly reproduced by all models. The same test case will be addressed later in the present work.

Chapter 3

Numerical Methodology: The DLR-TAU code

All simulations in the present work were performed by the DLR-TAU code. The DLR-TAU code (hereafter referred to as TAU) is a CFD software package developed at the German Aerospace Center (DLR), which mainly consists of a compressible finite-volume flow solver for hybrid unstructured grids, see e.g., Schwamborn et al. (2006) for an overview. TAU is based on cell-vertex type finite-volume discretization and uses the dual-grid approach. In the preprocessing step, the dual-grid is constructed from the primary grid and then treated as control volumes for the finite-volume discretization. In Section 3.1, the governing equations used in TAU will be described. In Section 3.2, the RANS turbulence models used in the present work will be described in detail. In Section 3.3, the dual-grid approach and the discretization schemes of the governing equations will be explained.

3.1 Governing Equations

3.1.1 Compressible Navier-Stokes Equations

The governing equations of fluids consist of conservation of mass, momentum and energy. The differential form of these equations for compressible flows are written as follows:

$$\frac{\partial \rho}{\partial t} + \frac{\partial}{\partial x_i}(\rho u_i) = 0, \tag{3.1}$$

$$\frac{\partial}{\partial t}(\rho u_i) + \frac{\partial}{\partial x_j}(\rho u_j u_i) = -\frac{\partial p}{\partial x_i} + \frac{\partial \tau_{ij}^v}{\partial x_j}, \tag{3.2}$$

$$\frac{\partial}{\partial t}(\rho E) + \frac{\partial}{\partial x_j}(\rho u_j H) = \frac{\partial}{\partial x_j}\left(u_i \tau_{ij}^v\right) - \frac{\partial q_j}{\partial x_j}, \tag{3.3}$$

where ρ denotes density, u_i velocity components, p pressure, τ_{ij}^v viscous stress tensor, E total energy per unit volume, H total enthalpy per unit volume and q_j heat flux vector. The subscript $i, j = (1, 2, 3)$ stands for x-, y-, z-direction, respectively.

Total energy E and total enthalpy H are defined as

$$E = e + \frac{1}{2}u_i u_i, \tag{3.4}$$

$$H = h + \frac{1}{2}u_i u_i = e + \frac{p}{\rho} + \frac{1}{2}u_i u_i = E + \frac{p}{\rho}, \tag{3.5}$$

where e denotes internal energy per unit volume, h enthalpy per unit volume. Here we assume the perfect gas.

The heat flux vector is obtained from Fourier's law:

$$q_j = -\kappa \frac{\partial T}{\partial x_j}, \tag{3.6}$$

where κ denotes thermal conductivity and T temperature.

The viscous stress tensor τ_{ij}^v are defined as

$$\tau_{ij}^v = 2\mu S_{ij} + \lambda \frac{\partial v_k}{\partial x_k}\delta_{ij} = 2\mu S_{ij} - \left(\frac{2\mu}{3}\right)\frac{\partial v_k}{\partial x_k}\delta_{ij}, \tag{3.7}$$

where S_{ij} is strain-rate tensor, λ the second coefficient of viscosity and δ_{ij} the Kronecker delta. The Stokes's hypothesis is used for the second term. The definition of strain-rate tensor is as follows:

$$S_{ij} = \frac{1}{2}\left(\frac{\partial u_i}{\partial x_j} + \frac{\partial u_j}{\partial x_i}\right). \tag{3.8}$$

3.1.2 Compressible Reynolds-Averaged Navier-Stokes Equations

The idea behind the Reynolds-Averaged Navier-Stokes (RANS) equations is Reynolds decomposition, where flow variables are decomposed into a mean and a fluctuating part. For example, velocity component u_i can be represented as

$$u_i = \bar{u}_i + u_i', \tag{3.9}$$

where the mean part is denoted by an overbar and the fluctuation part by a prime. Note that the mean of a fluctuation part is zero, i.e., $\overline{u_i'} = 0$. For compressible flows where density is not constant,

Favre averaging (also called mass-weighted averaging) is often used instead of Reynolds averaging in order to simplify the equations. The Favre averaging for a quantity f is performed as follows:

$$f = \tilde{f} + f'', \quad \tilde{f} = \frac{\overline{\rho f}}{\bar{\rho}}, \tag{3.10}$$

where a Favre-averaged part is denoted by a tilde and a fluctuating part by double prime. Note that the Favre average of the fluctuating part is again zero, but the Reynolds average of the fluctuation part here is nonzero, i.e., $\widetilde{u_i''} = 0, \overline{u_i''} \neq 0$. Usually, the density and the pressure are Reynolds-averaged, and velocity and thermodynamic variables are Favre-averaged. The Favre- and Reynolds-averaged compressible Navier-Stokes equations are

$$\frac{\partial \bar{\rho}}{\partial t} + \frac{\partial}{\partial x_i}\left(\bar{\rho}\tilde{u}_i\right) = 0 \tag{3.11}$$

$$\frac{\partial}{\partial t}\left(\bar{\rho}\tilde{u}_i\right) + \frac{\partial}{\partial x_j}\left(\bar{\rho}\tilde{u}_j\tilde{u}_i\right) = -\frac{\partial \bar{p}}{\partial x_i} + \frac{\partial}{\partial x_j}\left(\bar{\tau}_{ij} - \bar{\rho}\widetilde{u_i''u_j''}\right) \tag{3.12}$$

$$\begin{aligned}\frac{\partial}{\partial t}(\bar{\rho}\tilde{E}) + \frac{\partial}{\partial x_j}\left(\bar{\rho}\tilde{u}_j\tilde{H}\right) &= \frac{\partial}{\partial x_j}\left(-\tilde{q}_j - \bar{\rho}\widetilde{u_j''h''} + \widetilde{\tau_{ij}u_i''} - \bar{\rho}\widetilde{u_j''k}\right) \\ &\quad + \frac{\partial}{\partial x_j}\left[\tilde{u}_i\left(\tilde{\tau}_{ij} - \bar{\rho}\widetilde{u_i''u_j''}\right)\right].\end{aligned} \tag{3.13}$$

Here, the Favre-averaged Reynolds stress tensor is written as

$$\tau_{ij}^F = \bar{\rho}\widetilde{R}_{ij} = -\bar{\rho}\widetilde{u_i''u_j''}. \tag{3.14}$$

Considering the symmetric property of the Reynolds stress tensor, one can understand that six additional unknown variables are added to the set of governing equations. Due to the introduction of these six unknowns, the governing equations can no longer be solved without modelings. This leads to the necessity of turbulence modelings which will be discussed in the following section.

3.2 Turbulence Models

3.2.1 Treatments of the Reynolds Stress Tensor

RANS turbulence models out there can be classified by how the Reynolds stress tensor is treated. The simplest approach is the so-called linear eddy viscosity model (EVM), where the Reynolds stress tensor is modeled via the Boussinesq hypothesis

$$\bar{\rho}\widetilde{R}_{ij} = -2\mu_t\widetilde{S}_{ij}^* + \frac{2}{3}\bar{\rho}\tilde{k}\delta_{ij} \tag{3.15}$$

with the traceless strain tensor $\tilde{S}^*_{ij}$ defined as follows

$$\tilde{S}_{ij} = \frac{1}{2}\left(\frac{\partial \widetilde{u}_i}{\partial x_j} + \frac{\partial \widetilde{u}_j}{\partial x_i}\right), \tag{3.16}$$

$$\tilde{S}^*_{ij} = \widetilde{S}_{ij} - \frac{1}{3}\widetilde{S}_{kk}\delta_{ij}. \tag{3.17}$$

The linear eddy viscosity model is the base of many common turbulence models, including the Spalart-Allmaras type models and k-ω type models, which will be described in the following.

Another approach is to directly evaluate the Reynolds stress tensor by solving their transport equations. This approach is called the differential Reynolds stress model.

3.2.2 The Spalart-Allmaras One Equation Model

The Spalart-Allmalas (SA) model is the method that solves the transport equation of $\tilde{\nu}$ instead of solving for the original turbulent eddy viscosity ν. The relationships between $\tilde{\nu}$ and ν are as follows:

$$\nu_t = \frac{\mu_t}{\bar{\rho}} = \tilde{\nu} f_{v1} \tag{3.18}$$

$$f_{v1} = \frac{\chi^3}{\chi^3 + c_{v1}^3}, \quad \chi = \frac{\tilde{\nu}}{\bar{\nu}}, \quad c_{v1} = 7.1 \tag{3.19}$$

with $\bar{\nu}$ the average kinematic viscosity.

The general formulation of transport equation of $\tilde{\nu}$ is given by

$$\frac{\partial(\bar{\rho}\tilde{\nu})}{\partial t} + \frac{\partial}{\partial x_j}\left(\bar{\rho}\tilde{\nu}\tilde{u}_j\right) = \bar{\rho}P^{(\tilde{\nu})} - \bar{\rho}D^{(\tilde{\nu})} - \bar{\rho}\Phi^{(\tilde{\nu})} + \left(\bar{\rho}C^{(\tilde{\nu})}\right) + \left(\bar{\rho}T^{(\tilde{\nu})}\right), \tag{3.20}$$

where $\bar{\rho}P^{(\tilde{\nu})}$ denotes the production term, $\bar{\rho}D^{(\tilde{\nu})}$ the diffusion term, and $\bar{\rho}\Phi^{(\tilde{\nu})}$ the wall destruction term. $\bar{\rho}C^{(\tilde{\nu})}$ and $\bar{\rho}T^{(\tilde{\nu})}$ are the modification terms for compressibility and turbulence onset respectively. These terms are treated optionally.

The first three terms are given as follows:

$$\bar{\rho}P^{(\widetilde{\nu})} = c_{b1}\left(1 - f_{t2}\right)\widetilde{S}\bar{\rho}\widetilde{\nu}, \tag{3.21}$$

$$\bar{\rho}D^{(\widetilde{\nu})} = \frac{1}{\sigma}\left\{\frac{\partial}{\partial x_j}\left[\bar{\rho}(\bar{\nu} + \widetilde{\nu})\frac{\partial \widetilde{\nu}}{\partial x_j}\right] + c_{b2}\bar{\rho}\frac{\partial \widetilde{\nu}}{\partial x_j}\frac{\partial \widetilde{\nu}}{\partial x_j}\right\}, \tag{3.22}$$

$$\bar{\rho}\Phi^{(\widetilde{\nu})} = \left(c_{w1}f_w - \frac{c_{b1}}{\kappa^2}f_{t2}\right)\bar{\rho}\left[\frac{\widetilde{\nu}}{d}\right]^2, \tag{3.23}$$

$$\tag{3.24}$$

where each function is given by

$$
\begin{aligned}
f_{t2} &= c_{t3} \exp\left(-c_{t4}\,\chi^2\right)\,, \\
\tilde{S} &= S + \frac{\tilde{\nu}}{\kappa^2 d^2} f_{v2}\,, \quad S = \sqrt{2\Omega_{ij}\Omega_{ij}} = \sqrt{\frac{1}{2}\left(\frac{\partial u_i}{\partial x_j} - \frac{\partial u_j}{\partial x_i}\right)^2}\,, \\
f_{v2} &= 1 - \frac{\chi}{1+\chi f_{v1}}\,, \quad f_w = g\left(\frac{1+c_{w3}^6}{g^6+c_{w3}^6}\right)^{1/6}\,, \\
g &= r + c_{w2}(r^6 - r)\,, \quad r = \min\left[\frac{\tilde{\nu}}{\tilde{S}\kappa^2 d^2}, 10\right]
\end{aligned}
\tag{3.25}
$$

and the constants are summarized as follows:

$$
\begin{aligned}
&c_{b1} = 0.1335\,, \quad \sigma = 2/3\,, \quad c_{b2} = 0.622\,, \\
&\kappa = 0.41\,, \quad c_{w1} = \frac{c_{b1}}{\kappa^2} + \frac{1+c_{b2}}{\sigma}\,, \quad c_{w2} = 0.3\,, \quad c_{w3} = 2 \\
&c_{t3} = 1.2\,, \quad c_{t4} = 0.5
\end{aligned}
\tag{3.26}
$$

In the production term, the modified vorticity $\tilde{S}$ is responsible for controlling the rate of production. The f_{t2} decreases the production near a laminar region according to the value of χ.

The wall destruction term describes the effect that eddies are destructed due to the presence of a wall. The viscous effect of the wall destroys eddies near the wall. Also, the pressure fluctuation is blocked by the presence of a wall. Since this effect becomes weaker as going away from the wall, the destruction term is proportional to $1/d^2$, where d is the distance from the wall.

The diffusion term consists of the linear part and the additional nonlinear part. The nonlinear part is important to get an accurate result near the boundary of the turbulent region since therein the diffusion effect is dominant.

In this work, we use the model classified as SA-neg in the NASA Turbulence Modeling Resource (TMR) website (`https://turbmodels.larc.nasa.gov/`). This model was originally developed to deal with the situation where the viscosity takes a non-physical negative value. This happens quite often when the grids are coarse, or the flow is transient. To handle this issue, the SA-neg model uses other forms for the production term, the diffusion term, and wall destruction term in the case of $\tilde{\nu} < 0$. The standard SA model is used for $\tilde{\nu} \leq 0$.

$$\bar{\rho} P_n^{(\widetilde{\nu})} = c_{b1}\,(1 - c_{t3})\,S\bar{\rho}\widetilde{\nu}, \tag{3.27}$$

$$\bar{\rho} D_n^{(\widetilde{\nu})} = \frac{1}{\sigma}\left\{\frac{\partial}{\partial x_j}\left[\bar{\rho}(\bar{\nu} + f_n\widetilde{\nu})\frac{\partial \widetilde{\nu}}{\partial x_j}\right]\right\}, \tag{3.28}$$

$$\bar{\rho}\Phi_n^{(\widetilde{\nu})} = -c_{w1}\bar{\rho}\left[\frac{\widetilde{\nu}}{d}\right]^2, \tag{3.29}$$

$$\tag{3.30}$$

with

$$f_n = \frac{c_{n1} + \chi^3}{c_{n1} - \chi^3}, \quad c_{n1} = 16. \tag{3.31}$$

Notice that the modified production term is herein defined in terms of the vorticity S, and the wall destruction term takes the negative sign.

3.2.3 Two-Equation k-ω Shear Stress Transport (SST) Model

The k-ω SST model is the method where two transport equations for the specific turbulent kinetic energy k and the specific dissipation rate ω are solved to close the RANS equations. The model is widely understood as a combination of the classical k-ω model by Wilcox (1988) and the k-ϵ model by Jones and Launder (1972). The idea is presented by Menter (1994) in order to overcome the freestream sensitivity of the original k-ω model while keeping the good predictive performance near walls. In his paper, two models are proposed; one is the so-called Menter Baseline (BSL) model, and the other is Menter Shear Stress Transport (SST) model. The SST model uses a modified definition of the eddy viscosity to account for the effect of the transport of the principal turbulent shear stress. The SST is widely used in the CFD community due to its strength in predicting adverse pressure gradient flows.

The two turbulence equations in the compressible form used in TAU are as follows.

k-equation

$$\frac{\partial(\bar{\rho}\tilde{k})}{\partial t} + \frac{\partial}{\partial x_j}\left(\bar{\rho}\widetilde{k}\widetilde{u}_j\right) = \bar{\rho}P^{(\tilde{k})} - \bar{\rho}\varepsilon + \bar{\rho}D^{(\tilde{k})} \tag{3.32}$$

where $\bar{\rho}P^{(\tilde{k})}$ is the production term, $\bar{\rho}\varepsilon$ the dissipation term, and $\bar{\rho}D^{(\tilde{k})}$ the diffusion term. Note that the turbulent kinetic energy is given as a half of the trace of the Reynolds stress tensor

$$\bar{\rho}\tilde{k} = \frac{1}{2}\bar{\rho}\widetilde{R}_{kk}. \tag{3.33}$$

Each term is defined as follows:

$$\bar{\rho}P^{(\tilde{k})} = -\bar{\rho}\widetilde{R}_{ij}\frac{\partial\widetilde{u}_i}{\partial x_j} = 2\mu^{(t)}\tilde{S}^{\tilde{4}}_{ij}\frac{\partial\widetilde{u}_i}{\partial x_j} - \frac{2}{3}\bar{\rho}\tilde{k}\frac{\partial\widetilde{u}_k}{\partial x_k} = 2\mu^{(t)}\tilde{S}^{*}_{ij}\tilde{S}_{ij} - \frac{2}{3}\bar{\rho}\tilde{k}\frac{\partial\widetilde{u}_k}{\partial x_k}, \tag{3.34}$$

$$\bar{\rho}\varepsilon = \beta^{(\tilde{k})}\bar{\rho}\tilde{k}\omega, \tag{3.35}$$

$$\bar{\rho}D^{(\tilde{k})} = \frac{\partial}{\partial x_j}\left[\left(\bar{\mu} + \sigma^{(\tilde{k})}\mu^{(t)}\right)\frac{\partial\widetilde{k}}{\partial x_j}\right], \tag{3.36}$$

where $\beta^{(\tilde{k})}$ and $\sigma^{(\tilde{k})}$ are closure coefficients, and $\mu^{(t)}$ the eddy viscosity.

ω-equation

$$\frac{\partial(\bar{\rho}\omega)}{\partial t} + \frac{\partial}{\partial x_j}\left(\bar{\rho}\omega\widetilde{u}_j\right) = \bar{\rho}P^{(\omega)} - \bar{\rho}\Phi^{(\omega)} + \bar{\rho}C_D^{(\omega)} + \bar{\rho}D^{(\omega)} \tag{3.37}$$

where $\bar{\rho}P^{(\omega)}$ is the production term, $\bar{\rho}\Phi^{(\omega)}$ the dissipation term, $\bar{\rho}C_D^{(\omega)}$ the cross-diffusion term, and $\bar{\rho}D^{(\omega)}$ the diffusion term.

Each term is defined as follows:

$$\bar{\rho}P^{(\omega)} = \gamma^{(\omega)} S_c^{(\omega)} \bar{\rho}P^{(\tilde{k})}, \tag{3.38}$$

$$\bar{\rho}\Phi^{(\omega)} = \beta^{(\omega)}\bar{\rho}\omega^2, \tag{3.39}$$

$$\bar{\rho}C_D^{(\omega)} = \sigma^{(d)}\frac{\bar{\rho}}{\omega}\frac{\partial\widetilde{k}}{\partial x_k}\frac{\partial\omega}{\partial x_k}, \tag{3.40}$$

$$\bar{\rho}D^{(\omega)} = \frac{\partial}{\partial x_j}\left[\left(\bar{\mu} + \sigma^{(\omega)}\mu^{(t)}\right)\frac{\partial\omega}{\partial x_j}\right], \tag{3.41}$$

where $\gamma^{(\omega)}$, $\beta^{(\omega)}$, $\sigma^{(d)}$ and $\sigma^{(\omega)}$ are closure coefficients, $S_c^{(\omega)}$ is called scaling of the production term, and $\mu^{(t)}$ the eddy viscosity. The definition of $S_c^{(\omega)}$ is given by

$$S_c^{(\omega)} = \frac{\omega}{\widetilde{k}} \equiv \frac{\bar{\rho}}{\mu^{(t)}}. \tag{3.42}$$

As mentioned previously, Menter's BSL and SST model are understood as a combination of k-ω model by Wilcox and the k-ϵ model. This is due to that fact that the closure coefficients are smoothly changed between the near wall region and the freestream region with the help of a blending function.

$$\phi = F_1\phi_i + (1 - F_1)\,\phi_o, \tag{3.43}$$

where ϕ being six closure coefficients, F_1 the blending function, and the subscripts i and o stand for the near wall region ('inner' region) and the freestream region ('outer' region), respectively. The blending function is given by

$$F_1 = \tanh(G_1^4), \tag{3.44}$$

where

$$G_1 = \min\left[\max\left(\Gamma_1, \Gamma_2\right), \Gamma_3\right], \tag{3.45}$$

with

$$\Gamma_1 = \frac{\sqrt{k}}{0.09\omega d}, \tag{3.46}$$

$$\Gamma_2 = \frac{500\bar{\mu}}{\bar{\rho}\omega d^2}, \tag{3.47}$$

$$\Gamma_3 = \frac{2\sigma_o^{(d)}\bar{\rho}k}{\bar{\rho}C_{D,o}^{(\omega)}d^2}, \tag{3.48}$$

and

$$\bar{\rho}C_{D,o}^{(\omega)} = \max\left(\sigma_o^{(d)}\frac{\bar{\rho}}{\omega}\frac{\partial\tilde{k}}{\partial x_k}\frac{\partial\omega}{\partial x_k}, 10^{-20}\right). \tag{3.49}$$

The definition of the eddy viscosity for the original $k-\omega$ model by Wilcox (1988) and also for the BSL model is given by

$$\mu^{(t)} = \frac{\bar{\rho}\tilde{k}}{\omega}. \tag{3.50}$$

As stated previously, the SST model uses a modified definition of the eddy viscosity. This is intended to improve its sensitivity to adverse pressure gradients. The eddy viscosity in SST is defined as

$$\mu^{(t)} = \frac{\bar{\rho}\tilde{k}a_1}{\max\left(a_1\omega, \Omega F_2\right)} = \frac{\bar{\rho}\widetilde{k}}{\omega}\frac{1}{\max\left(1, \frac{\Omega}{\omega}\frac{F_2}{a_1}\right)}, \tag{3.51}$$

where

$$a_1 = 0.31, \quad F_2 = \tanh(G_2^2), \quad G_2 = \max(2\Gamma_1, \Gamma_2). \tag{3.52}$$

The parameters Γ_1 and Γ_2 are the same as the ones used in the blending function F_1.

Here, Ω is called a scalar velocity gradient parameter, and two different definitions have been published by Menter. The first version Menter SST 1994 (Menter (1994)) uses the definition by vorticity

$$\Omega = \sqrt{2\widetilde{\Omega}_{ij}\widetilde{\Omega}_{ij}}, \tag{3.53}$$

while the later published version Menter SST 2003 (Menter et al. (2003)) is based on strain rate

$$\Omega = \sqrt{2\widetilde{S}_{ij}\widetilde{S}_{ij}}. \tag{3.54}$$

Lastly, the closure coefficients are summarized in Table 3.1. It should be noted that the closure coefficients in TAU follow a publication by Menter and Rumsey (1994).

	$\beta^{(\tilde{k})}$	$\beta^{(\omega)}$	$\sigma^{(\tilde{k})}$	$\sigma^{(\omega)}$	$\gamma^{(\omega)}$	$\sigma^{(d)}$
Inner region (k-ω part)	0.09	0.0752	0.85	0.5	0.5555555	0
Outer region (k-ε part)	0.09	0.0828	1.0	0.857	0.440	1.714

Table 3.1: Closure coefficients of Menter SST model in TAU

3.2.4 SSG/LRR-ω Reynolds Stress Model

The Reynolds stress models (RSM) are the models where the Reynolds stresses are directly treated by solving their transport equations without the Boussinesq hypothesis. The SSG/LRR-ω RSM is one of the most successful RSM, especially in the aerospace field, and it has been verified and validated by NASA and DLR based on the test cases on the Turbulence Modeling Resource (TMR) website (Eisfeld et al. (2016)). What the SSG/LRR-ω model differentiates with other RSMs is the treatment of the pressure-strain correlation term, which will be described in the following. The SSG/LRR-ω model combines the formulation by Speziale-Sarkar-Gatski (SSG) (Speziale et al. (1991)) and the one by Launder, Reece, and Rodi (LRR) (Launder et al. (1975)) through blending of the model coefficients, in analogy to Menter's BSL and SST model. The SSG formulation is based on dissipation ε, which is used for the freestream region, and the LRR model is based on ω, which is used for the near-wall area.

Firstly, the Reynolds stress transport equation is given by

$$\frac{\partial\left(\bar{\rho}\tilde{R}_{ij}\right)}{\partial t}+\frac{\partial}{\partial x_k}\left(\bar{\rho}\tilde{R}_{ij}\tilde{u}_k\right)=\bar{\rho}P_{ij}+\bar{\rho}\Pi_{ij}-\bar{\rho}\varepsilon_{ij}+\bar{\rho}D_{ij}, \tag{3.55}$$

where $\bar{\rho}\tilde{R}_{ij}$ being the Reynolds stress tensor, $\bar{\rho}P_{ij}$ the production term, $\bar{\rho}\Pi_{ij}$ the pressure-strain correlation term, $\bar{\rho}\varepsilon_{ij}$ the dissipation term, and $\bar{\rho}D_{ij}$ the diffusion term.

The production term does not need any modelings and is given by

$$\bar{\rho}P_{ij}=-\bar{\rho}\tilde{R}_{ik}\frac{\partial\tilde{u}_j}{\partial x_k}-\bar{\rho}\tilde{R}_{jk}\frac{\partial\tilde{u}_i}{\partial x_k}. \tag{3.56}$$

The pressure-strain correlation term is modeled as follows due to Speziale, Sarkar, and Gatski (SSG) (Speziale et al. (1991))

$$\begin{aligned}\bar{\rho}\Pi_{ij}=&-\left(C_1\bar{\rho}\varepsilon+\frac{1}{2}C_1^*\bar{\rho}P_{kk}\right)\tilde{b}_{ij}+C_2\bar{\rho}\varepsilon\left(\tilde{b}_{ik}\tilde{b}_{kj}-\frac{1}{3}\tilde{b}_{kl}\tilde{b}_{kl}\delta_{ij}\right)\\&+\left(C_3-C_3^*\sqrt{\tilde{b}_{kl}\tilde{b}_{kl}}\right)\bar{\rho}\tilde{k}\tilde{S}_{ij}^*+C_4\bar{\rho}\tilde{k}\left(\tilde{b}_{ik}\tilde{S}_{jk}+\tilde{b}_{jk}\tilde{S}_{ik}-\frac{2}{3}\tilde{b}_{kl}\tilde{S}_{kl}\delta_{ij}\right)\\&+C_5\bar{\rho}\tilde{k}\left(\tilde{b}_{ik}\tilde{W}_{jk}+\tilde{b}_{jk}\tilde{W}_{ik}\right)\end{aligned} \tag{3.57}$$

where b_{ij} is an anisotropy tensor and $\tilde{W}_{ij}$ the rotation tenor, which are respectively represented as

$$\tilde{b}_{ij} = \frac{\tilde{R}_{ij}}{2\tilde{k}} - \frac{1}{3}\delta_{ij}, \tag{3.58}$$

$$\tilde{W}_{ij} = \frac{1}{2}\left(\frac{\partial \tilde{u}_i}{\partial x_j} - \frac{\partial \tilde{u}_j}{\partial x_i}\right). \tag{3.59}$$

Also, C_i and C_i^* are model-dependent coefficients. As mentioned earlier, these coefficients and the above SSG formulation are blended with the LRR model. See Eisfeld et al. (2016), Eisfeld (2019) for the values of coefficients.

The dissipation term is simply modeled as an isotropic tensor

$$\bar{\rho}\varepsilon_{ij} = \frac{2}{3}\bar{\rho}\varepsilon\delta_{ij}. \tag{3.60}$$

The isotropic dissipation rate ε can be formulated as

$$\varepsilon = C_\mu \tilde{k}\omega \tag{3.61}$$

in which $C_\mu = 0.09$. In order to calculate this quantity, the value of ω is necessary. For this purpose, the ω-equation by Menter's BSL model is introduced and solved together with the Reynolds stress transport equations.

The diffusion term has two model formulations. One is so-called simple gradient diffusion (Shir (1973)) and the other is generalized gradient diffusion (Daly (1970)). In the present work, the simple gradient diffusion version is used for all simulations. The formulation is given by

$$\bar{\rho}D_{ij} = \frac{\partial}{\partial x_k}\left[\left(\bar{\mu} + \frac{D^{(\mathrm{SD})}}{C_\mu}\frac{\bar{\rho}\tilde{k}^2}{\varepsilon}\right)\frac{\partial \tilde{R}_{ij}}{\partial x_k}\right], \tag{3.62}$$

with a mode coefficient $D^{(\mathrm{SD})}$ whose value should also be referred to (Eisfeld et al., 2016).

3.3 Discretizaiton Scheme

3.3.1 Discretization of Computational Domain

The discretization strategy in TAU is a cell-vertex type finite-volume scheme with dual control volumes. In TAU, the flow variables are stored at the vertices of the primary grid, which is a grid generated by an external grid generation tool and imported into TAU. The so-called dual-grid is created in the pre-processing step by connecting the centroids of the primary grid cells, and the dual grid cells are used as control volumes for the finite-volume discretization of the governing equations. An example of the primary grid and accordingly generated dual grid is illustrated in Fig. 3.1.

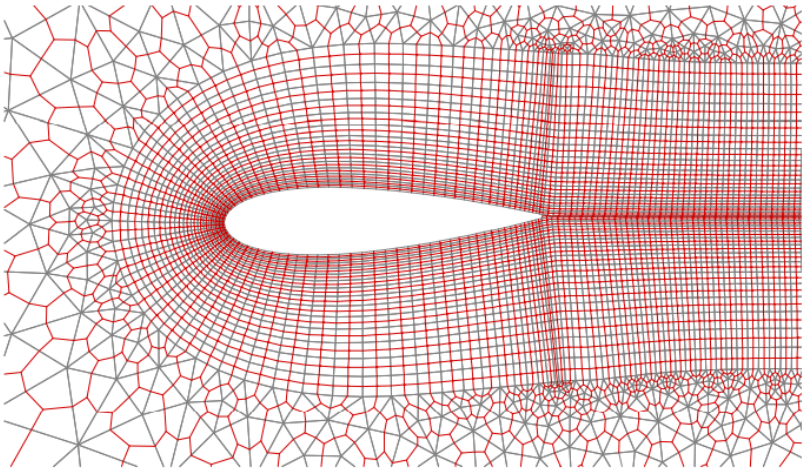

Fig. 3.1: Exemplary hybrid primary grid (black) and the corresponding dual grid (red) around a NACA-0021 airfoil (Reuß (2015))

3.3.2 Spatial Discretization

The integral form of the governing equations in the computational domain Ω can generally be written as

$$\frac{\partial}{\partial t}\int_{\Omega}\vec{W}d\Omega + \oint_{\partial\Omega}\left(\vec{F}^{c} - \vec{F}^{v}\right)dS = \int_{\Omega}\vec{Q}d\Omega, \tag{3.63}$$

where $\vec{W}$ being the conservative variables, $\vec{F}^{c}$ the convective fluxes, $\vec{F}^{v}$ the viscous fluxes, and $\vec{Q}$ the source term. Applying the finite-volume discretization, for a control volume V_I the equations read

$$\frac{\partial\vec{W}_I}{\partial t} = -\frac{1}{V_I}\sum_{J}\left(\vec{F}^{c}_{IJ} - \vec{F}^{v}_{IJ}\right)\Delta S_{IJ} + \vec{Q}_I, \tag{3.64}$$

where J stands for the indices for the adjacent control volumes. In CFD computations, the selection of the discretization schemes for convective fluxes is of great importance.

Central Scheme with Artificial Dissipation

A central scheme is a method where the fluxes at a cell face are computed from the arithmetic average of the conservative variables on both sides of the face. This would allow numerical instabilities such as odd-even decoupling or overshoots at shocks, and therefore artificial dissipation has to be added for the scheme's stability. The central fluxes can be approximated by different approaches such as an

average of fluxes, an average of variables, the skew-symmetric Kok scheme (Kok (2009)), and so on. With the average of flux approach as an example, the convective fluxes are computed as

$$\vec{F}^c_{IJ} \approx \frac{1}{2}\left(\vec{F}^c_I + \vec{F}^c_J\right) - \frac{1}{2}\tilde{\alpha}\vec{D}_{IJ} \tag{3.65}$$

with the artificial dissipative flux $\vec{D}_{IJ}$ and the artificial dissipation coefficient $\tilde{\alpha}$, which is either scalar dissipation or matrix dissipation. The dissipative fluxes for scalar dissipation are written as:

$$\vec{D}_{IJ} = \varepsilon^{k(2)} \cdot (\vec{W}_I - \vec{W}_J) - \varepsilon^{k(4)} \cdot \left(\nabla^2\vec{W}_I - \nabla^2\vec{W}_J\right), \tag{3.66}$$

where the coefficients $\varepsilon^{k(2)}, \varepsilon^{k(4)}$ are used to control the amount of dissipation to be added. The 2nd order dissipation coefficient $\varepsilon^{k(2)}$ is responsible for handling discontinuities, while the 4th order coefficient $\varepsilon^{k(4)}$ is for dissipation in smooth regions. For the scalar dissipation, $\tilde{\alpha}$ becomes the maximum eigenvalue of the flux Jacobian weighted by an additional term that accounts for grid stretching. With the matrix dissipation scheme, the solution accuracy can be improved by considering the full convective flux Jacobian, resulting in a more appropriate weighting of each dissipation term.

Due to the presence of stretched cells to resolve boundary layers and the demand for high accuracy, the Kok scheme with matrix dissipation is for the mean convective fluxes in the present work.

Upwind Scheme

Several upwind schemes are available in TAU. The upwind schemes are typically preferred over central schemes to improve the shock-capturing capability in the compressible regime. In the present study, which only deals with incompressible flows, however, Roe upwind scheme (Roe (1981)) is used for convective fluxes of turbulent equations according to the turbulence models for stability reasons.

3.3.3 Time Discretization

In addition to the spatial descretization, the time derivative of the governing equations must be treated. The Backward Euler implicit descretization scheme has been used together with the Lower-Upper Symmetric Gauss-Seidel (LU-SGS) iterative solver. The governing equations in general form read

$$\frac{\partial\vec{W}}{\partial t} = -\mathcal{R}(\vec{W}), \tag{3.67}$$

with the residual $\mathcal{R}(\vec{W})$. The steady state solution of the above equations is found by solving the time-dependent problem with pseudo-time t^* and seeking the solution where the residual becomes zero.

$$\frac{\partial\vec{W}}{\partial t^*} = -\mathcal{R}(\vec{W}) \longrightarrow 0 \tag{3.68}$$

The Backward Euler scheme is given by

$$\frac{\vec{W}^{n+1} - \vec{W}^{n}}{\Delta t^{*}} = -\mathcal{R}(\vec{W}^{n+1}), \tag{3.69}$$

where n represents the iteration step.

The LU-SGS scheme is based on the LDU factorization. Applying an approximate LDU factorization, the system matrix can be described in matrix notation as follows:

$$[\boldsymbol{L} + \boldsymbol{D}]\boldsymbol{D}^{-1}[\boldsymbol{D} + \boldsymbol{U}]\Delta\boldsymbol{W}^{n} = -\boldsymbol{R}^{n} \tag{3.70}$$

where

$$\Delta\boldsymbol{W}^{n} = \boldsymbol{W}^{n+1} - \boldsymbol{W}^{n}, \tag{3.71}$$

and $\boldsymbol{L}$ only consists of block terms in the strictly lower triangular matrix, $\boldsymbol{U}$ only consists of block terms in the strictly upper triangular matrix, and $\boldsymbol{D}$ is a diagonal matrix. This is solved by the following two steps:

$$\text{Forward sweep} : \Delta\boldsymbol{W}^{*} = \boldsymbol{D}^{-1}\left(-\boldsymbol{R}^{n} - \boldsymbol{L}\Delta\boldsymbol{W}^{*}\right) \tag{3.72}$$

$$\text{Backward sweep} : \Delta\boldsymbol{W}^{n} = \Delta\boldsymbol{W}^{*} - \boldsymbol{D}^{-1}\boldsymbol{U}\Delta\boldsymbol{W}^{n} \tag{3.73}$$

where $\Delta\boldsymbol{W}^{*}$ is an intermediate solution updated in the forward sweep.

Furthermore, in the present study, a multi-grid method is used to accelerate the convergence. Besides, a low-Mach number preconditioning is applied to obtain accurate solutions in the incompressible regime using the compressible flow solver TAU.

Chapter 4

The Virginia Tech Stability Wind Tunnel Experiment

This chapter describes the first test case, the Virginia Tech Stability Wind Tunnel (VTSWT) experiment. The experiment was performed in the framework of the NATO AVT-349 research project. The collaborative experimental and computational study of the experiment has been conducted within the subgroup of the larger NATO AVT-349 Research Technical Group, and its primary outcome was recently published (Fritsch et al. (2022)). The collaborative group consists of Virginia Tech, DLR, the University of Melbourne, Chalmers University of Technology, MARIN/IST, and the Sirehna Naval Group. The present thesis mainly addresses the computational efforts presented by DLR from this collaboration.

In the following, the experimental will firstly be described. Secondly, the computational set-ups, including the development of the computational grids and numerical methods, will be explained. Subsequently, the obtained results and the discussion will be presented.

4.1 Experimental set-ups

4.1.1 Flow Case

The experiments were conducted in the Virginia Tech Stability Wind Tunnel (VTSWT). The test section is a cuboid $1.85\,\mathrm{m} \times 1.85\,\mathrm{m}$ in cross section and 7.32m long in the streamwise direction. A contraction section exists in front of the test section, and a boundary layer trip is installed 3.584 m ahead of the entrance of the test section. A schematic view of the flow case and its coordinate system is illustrated in Fig. 4.1. Coordinate x is defined from the test section entrance, while the origin of coordinate y is defined on the port-side wall of the test section (bottom wall in Fig. 4.1). Coordinate z is defined such that $z = 0$ m represents the mid-plane of the wind tunnel. Hereafter, to avoid potential confusion, we refer to the port-side wall of the wind tunnel as 'bottom wall' and the starboard-side wall as 'top wall' unless otherwise noted. The boundary layer of our interest is the one developing

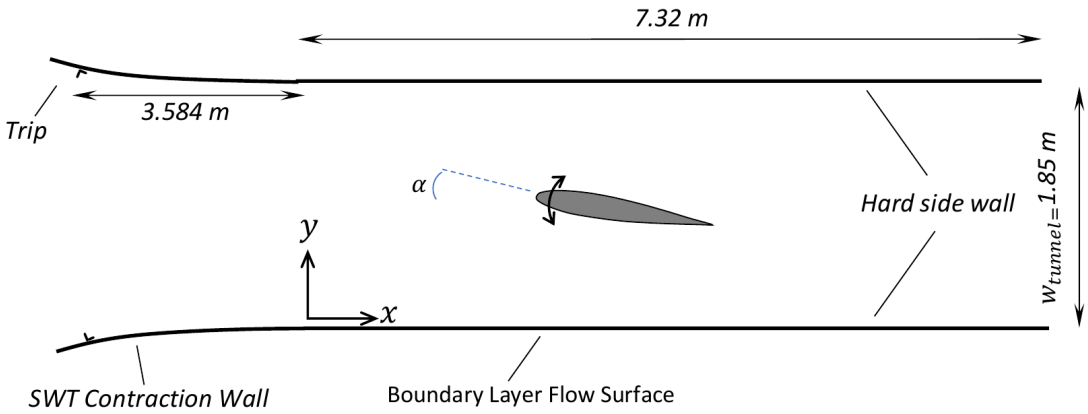

Fig. 4.1: Flow case set-up

on the bottom wall. A NACA0012 airfoil with 0.914 m chord length is installed in the test section, whose quarter chord is positioned nominally at $x = 3.44\,\mathrm{m}, y = 0.924\,\mathrm{m}$. Streamwise varying pressure distribution is generated on the walls of the test section by changing the angle of attack of the airfoil. The airfoil can be rotated nominally from -10 to 12 degrees. The experiment was conducted for two different Reynolds numbers, 2 million and 3.5 million, based on the airfoil chord length. Yet, this study only considers the 2 million case.

4.1.2 Measurement Techniques

Two different types of measurements were performed in the experiment. One is a rake of Pitot tubes technique, where 30 Pitot-probes are used to resolve the profiles of the boundary layers of interest. Fig. 4.2 shows the experimental set-up of the boundary layer rake. The mean velocity profiles are computed from the measured static pressure and the stagnation pressure values with the help of the incompressible Bernoulli's equation. The measurement positions are summarized in Table 4.1. The other method is a planar time-resolved Particle Image Velocimetry (TR-PIV). However, only rake measurement results are addressed in the present work. The comparisons between RANS simulations and PIV measurement data for turbulence quantities are presented in Fritsch et al. (2022).

Station	Streamwise position, x [m]
P3	1.253
P4	1.863
P5	2.472
P6	3.082
P7	3.691
P8	4.301
P9	4.911

Table 4.1: Rake probe measurement positions in the steramwise direction

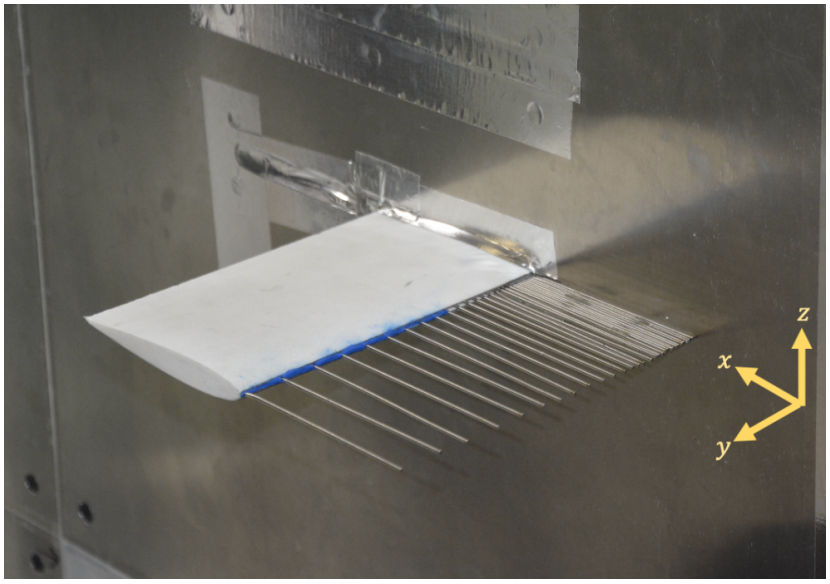

Fig. 4.2: A rake of Pitot tubes mounted on the port-side wall (bottom wall in Fig. 4.1).

4.1.3 Reference Point

Some of the important flow parameters, including skin friction coefficient and pressure coefficient, require a reference condition for their non-dimensionalization, and the selection of its reference is of great importance. In the early stage of the collaboration, the skin friction and pressure coefficients were calculated using the facility standard reference condition, which is based on a point in the contraction section. However, this point is not possible to probe in the developed computational grids. The reference point should be probable both in the experiments and the CFD computations for better comparisons. Therefore, a reference point has been chosen to be a pressure tap on the starboard wall (top wall in Fig. 4.1) located at $x = 1.47$ m , $y = 1.85$ m, $z = 0$ m. This location is far from the airfoil model, and therefore the effect of pressure gradients is expected to be fairly small. It should be noted that in the computational grid, this exact point is slightly out of the domain due to the inclination of the top wall, which will be explained in the following section. Thus, the nearest wall point around $y = 1.847$ m is probed in the computations.

4.2 Computational set-ups

4.2.1 Computational Grids

A common family of computational grids has been developed by Virginia Tech in order to provide consistency among the AVT-349 collaborators. Due to the two-dimensionality of the present flow case, two-dimensional grids have been selected, which provides computational cost benefits compared to three-dimensional set-ups. The finally developed grid set-up is described in Fig. 4.3. The wall on which the boundary layer of interest grows is modeled as a no-slip wall. On the other hand, the other side is modeled as a slip wall that is inclined by the angle of 0.46°. At first, a constant cross-section

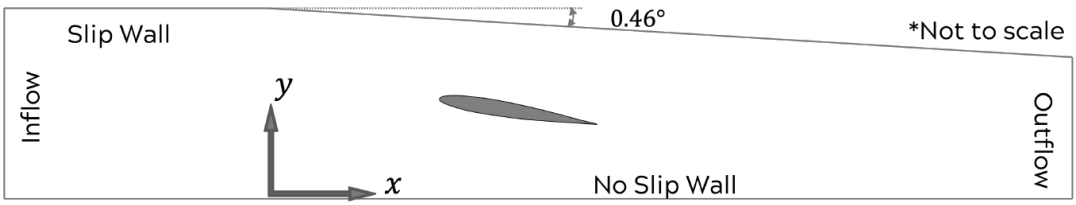

Fig. 4.3: Flow case set-up

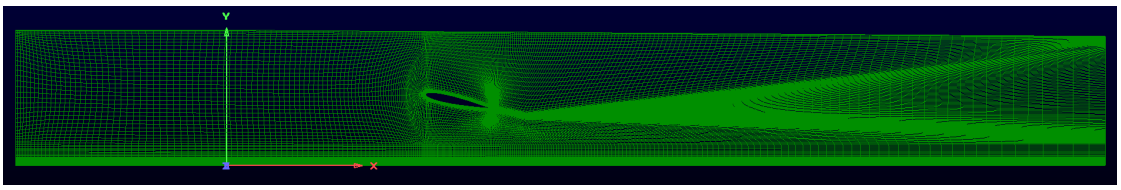

Fig. 4.4: Computational Grid for 12° (Level 5)

grid with two parallel no-slip walls was developed. However, it has been observed that this grid fails to reproduce the pressure gradients on the wall of interest, which must be captured accurately to discuss the effects of pressure gradients on turbulence models. This misprediction was presumably because the other two boundary layers developing on the floor and ceiling of VTSWT were not modeled in this naive 2D set-up. In the real experiment, these two other boundary layers effectively reduce the cross-sectional area of the wind tunnel, which can be seen as favorable pressure gradients. To remedy this issue, the starboard wall (top wall in Fig. 4.3) was modeled as a slip wall with 0.46° inclination to replicate the background FPG measured in the empty VTSWT. The contraction section is replaced by a constant-cross section inflow region, and its length was calibrated such that the inflow boundary layer parameters match with the experimental data.

The grid is fully structured, and the topology around the airfoil is a C-Grid type. Five different refinement levels were developed. The summary of the metrics is found in Table 4.2. The finest grid is Grid Level 1 (GL1). GL 3 was obtained by removing every other node of GL1 (refinement factor 2), and GL5 was from GL3 in the same manner. GL 2 and 4 were obtained by refining GL 3 and 5 respectively by a factor of $\sqrt{2}$. As an example, the coarsest grid for 12° can be found in Fig. 4.4.

In the present study, GL3 was selected for all simulations after conducting a grid convergence study. Fig. 4.5 shows the skin friction coefficient and pressure coefficient obtained using the SA-neg turbulence model for all refinement levels. As can be seen, the coarsest mesh GL5 is already fine enough to capture the same accurate level of C_f and C_p as GL1. Nevertheless, from GL3 on, an almost 'perfect' convergence is observed for these two quantities, and therefore, we decided to use GL3 for all simulations.

4.2.2 Numerical Methods

The numerical simulations were performed using the DLR-TAU code. The inviscid fluxes of the mean flow are computed by a second-order central differencing with artificial matrix-valued dissipation. Here the skew-symmetric Kok scheme is applied. For the turbulence equations, a second-order central scheme is used for one-equation turbulence models, whereas the first order Roe upwind scheme is

Grid Level	# Cells	Average Cell Area (m^2)	RMS Cell Area (m^2)
GL1	792,432	4.98×10^{-5}	9.07×10^{-5}
GL2	396,355	9.94×10^{-5}	1.81×10^{-4}
GL3	198,108	1.99×10^{-4}	3.64×10^{-4}
GL4	99,108	3.98×10^{-4}	7.27×10^{-4}
GL5	49,527	7.96×10^{-4}	1.46×10^{-3}

Table 4.2: Grid metrics of the 2D grid family

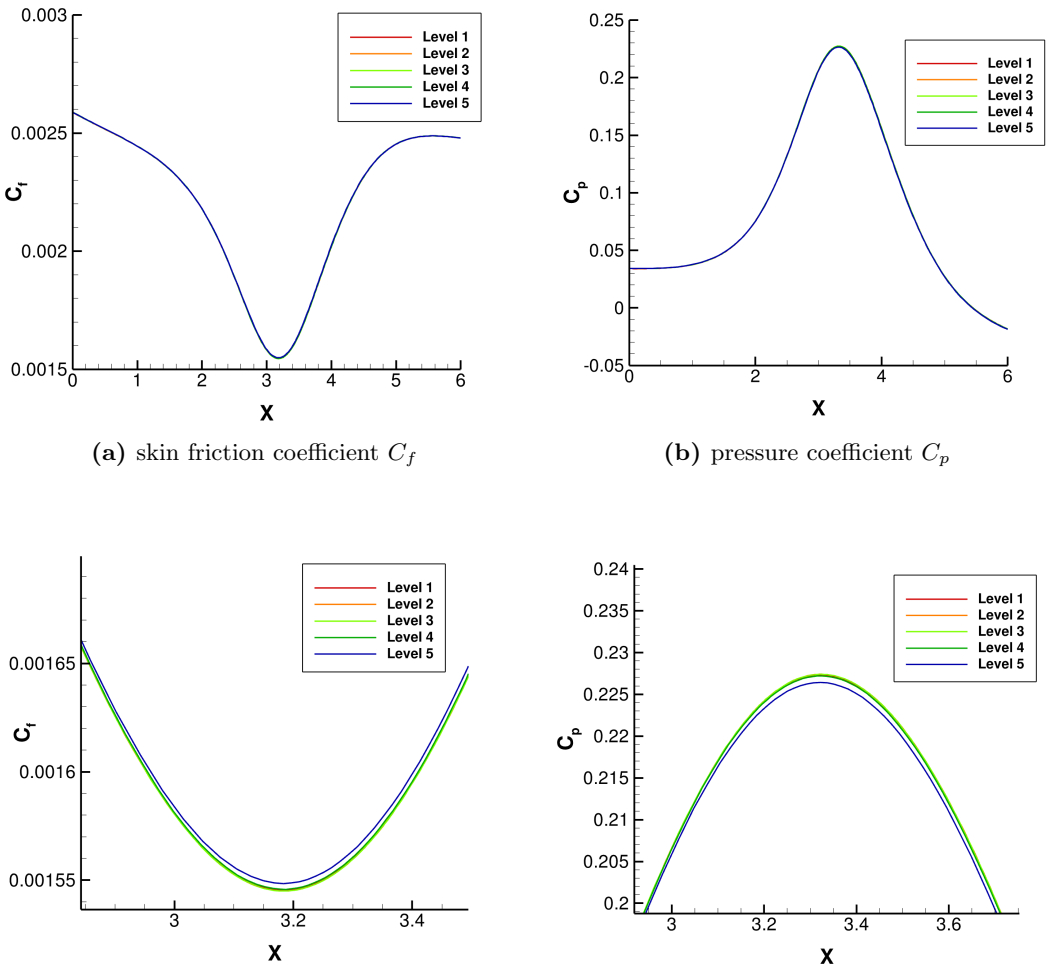

(a) skin friction coefficient C_f

(b) pressure coefficient C_p

(c) skin friction coefficient C_f (enlarged)

(d) pressure coefficient C_p (enlarged)

Fig. 4.5: Pressure and skin coefficients computed for the 12° case using SA-neg for five different grid levels.

Re_c	2.0×10^6
Characteristic Length	0.914 m
ρ	1.156 kg/m^3
μ	1.77×10^{-5} Pa $\cdot$ s
Turbulence Intensity	0.02 %
U_∞	33.5 m/s
q_∞	648.8 Pa
M_∞	0.099
p_∞	$94,272.0$ Pa
T_∞	284.1 K
$p_\mathbf{0}$	94922.4 Pa
$T_\mathbf{0}$	284.7 K
Altitude above Sea Level	604.4 m

Table 4.3: Reference conditions

applied for two-equation turbulence models and the differential Reynolds stress models. For a temporal discretization, an implicit backward Euler scheme solved with the lower-upper symmetric Gauss-Seidel (LU-SGS) scheme is used. In addition, due to the low Mach number of this test case, a low-Mach number preconditioning is applied in order to obtain accurate results using the compressible flow solver. Three different turbulence models have been compared in this test case: the negative SA model (SA-neg) (Allmaras and Johnson (2012)), the k-ω SST model (Menter et al. (2003)), and the SSG/LRR-ω Reynolds stress model (Eisfeld et al. (2016)).

The boundary conditions used in the numerical simulations are as follows. At the inlet of the computational domain, a so-called "reservoir-pressure inflow" boundary condition is applied, where the total pressure and total density are prescribed. A so-called "exit-pressure outflow" boundary condition is used at the outlet, where the static reference pressure is prescribed by default. A non-slip wall boundary is used on the bottom wall, and a slip-wall boundary is used on the top wall. The surface of the airfoil is treated as a non-slip wall.

The reference conditions used in the simulations are summarized in Table 4.3. These conditions are suggested based on the standard atmosphere conditions in Blacksburg, VA, USA, as well as a rough average of measured atmospheric conditions during experimental testing. It should be noted that these conditions may not provide a perfect dimensional matching with all experimental data since it was observed that ambient conditions changed over the course of the experimental campaign.

4.3 Results

In the present study, two extreme cases with the airfoil model at 12° and −10° are considered. A positive angle of attack generates an initially adverse pressure gradient, and after reaching the maximum, it turns out to be a favorable pressure gradient. In contrast, a negative angle of attack generates an initially favorable pressure gradient and then an adverse pressure gradient.

4.3.1 Boundary layer parameters

12° case

Fig. 4.6 shows the distribution of skin friction coefficient and pressure coefficient on the bottom wall. As can be seen, C_p increases until around $x = 3.5$ m and then continuously decreases downstream. It should be noted that there is no plateau in the pressure coefficient development. This is a unique feature of this test case, which provides a non-equilibrium feature of the flow. Overall, the CFD results of C_p show an excellent agreement with the experiment results. An exemption is observed near the entrance of the test section (between $x = 0$ m and $x = 1$ m); however, this is presumably attributed to the uncertainties (e.g., 3D effects) in the contraction section that are not addressed in this 2D set-up. Among the three turbulence models, the SST and SSG/LRR-ω results are almost perfectly overlapping with each other, while SA-neg gives a slight overprediction near the peak. Despite the small deviation of SA-neg, the fairly good agreement between the turbulence models suggest that the selection of the model does not influence the prediction of the freestream behaviors very much.

The skin friction coefficient shows an opposing trend to the pressure coefficient. In the adverse pressure gradient region, C_f decreases because the flow is decelerated, and the gradient of the mean velocity on the wall $dU/dy\,|_{y=0}$ becomes smaller. The opposite trend can be seen downstream, which can be explained in the same manner by the favorable pressure gradient and its acceleration (re-stabilization of the flow). The agreement between the experiment and the CFD solutions seems to be not as good as the pressure coefficient. All turbulence models underpredict C_f throughout the domain, and it seems that the deviation is enhanced as it goes downstream. The reason for the underprediction of C_f is difficult to identify. One possible source of this discrepancy is the misprediction of the mean velocity profile near the wall. As can be seen in Fig. 4.13, at P5 and P7, there is a noticeable difference in the mean velocity profile normalized by the edge velocity U_e between the experiment and the CFD results, while the agreement is fairly good at P3. This may explain the smaller discrepancy of C_f at P3 but the larger at P5. Having said that, other factors or their combination could be the main source of this discrepancy, such as the accuracy of the rake measurements near the wall, the 2D computational grid, slightly different reference values used for nondimensionalizing C_f (e.g., $\rho_{\mathrm{ref}}, U_{\mathrm{ref}}$), etc. For further discussions, more detailed PIV measurements near the wall and an improved computational set-up such as 3D computations would be necessary. These are planned as future works within the NATO AVT-349 community.

Fig. 4.7 shows the growth of boundary layer thicknesses and the shape factor. The boundary layer thicknesses increase gradually near the entrance, but the slope of their increment is enhanced due to the adverse pressure gradient from $x \approx 2.3$ m, and then reach their peaks. After reaching the maximum, they start to decrease because of the re-stabilization by the favorable pressure gradient.

The δ_{95} seems to be quite sensitive to turbulent models compared to displacement thickness δ^* and momentum thickness θ. Especially, the difference between the SA-neg and the other two is noticeable. This is attributed to the different shapes of the mean velocity profiles. A similar tendency can be observed in Fig. 4.13, where the curve of SA-neg is deviated from the other two models between $y/\delta_{95} = 0.4 - 0.8$, while the SST and SSG/LRR-ω are almost overlapping with each other. The turbulence model dependency in δ^* and θ is fairly small. This is probably because these are integral quantities, unlike δ_{95}, and the minor differences in the mean velocity profiles are masked.

The large variation in the shape factor $H = \delta^*/\theta$ is quite surprising considering the small variation in δ^* and θ respectively. Also, all turbulent models overpredict H throughout the domain, even at the first three stations where it looks like δ^* and θ are predicted quite well.

The reason for the large deviation in δ^* and θ after the forth station (between $x = 3 - 5$ m) is not yet clear. As mentioned in Fritsch et al. (2022), these results by DLR-TAU is an outliner compared to the other collaborators' results. The DLR-TAU's solution overpredicts δ^* and θ by around 5 % compared to the others. The difference could be attributed to the fact that TAU internally computes these quantities, while other collaborators evaluate these quantities in the postprocessing step. In principle, these should give the same result, but slight differences during the evaluation process might have resulted in this difference. Having said that, other collaborators' results also show a small overprediction of δ^* and θ between $x = 3 - 5$ m.

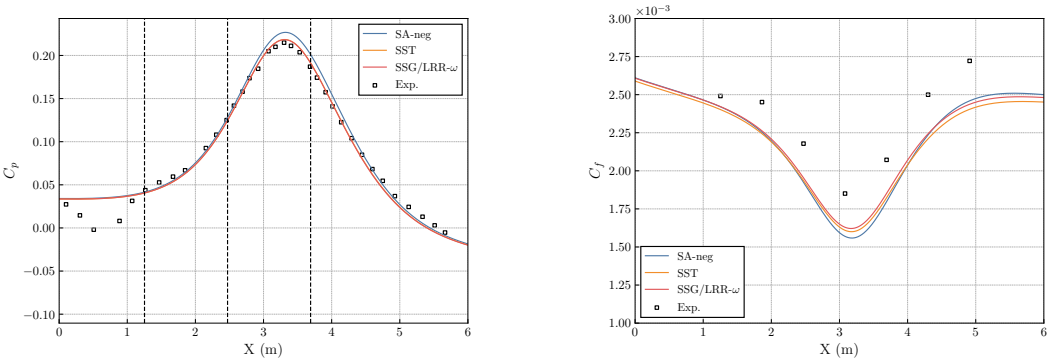

(a) pressure coefficient C_p **(b)** skin friction coefficient C_f

Fig. 4.6: Pressure and skin coefficients computed for the 12° case. The three vertical dashed lines in (a) represent the three rake measurement stations (P3, P5, and P7) where wall profiles are studied in the present work.

As mentioned earlier, this test case is expected to involve the non-equilibrium feature due to the continuously varying pressure gradient. Fig. 4.8 illustrates two different ways to show the degree of non-equilibriums. Fig. 4.8 (a) shows the development of the Rotta-Clauser pressure gradient parameter β. As can be observed, there is no region where β remains 0, which indicates that the flow is away from the equilibrium state. Also, the turbulence model dependency is quite small, yet this is not very surprising because the parameters incorporated in the definition of Rotta-Clauser parameter $\beta = (\delta^*/\tau_w)\, dP/dx$ do not show significant model dependencies as we already saw above. The agreement between the experimental results and the CFD results is relatively good in general. Here, however, careful interpretation is necessary. For example, at the last measurement station P9 in Fig. 4.8 (a), the experimental and computational results are fairly close. But this point is in fact where we observed a large overprediction of δ^* as seen in Fig. 4.7 (b). Besides, it should be reminded that C_f is underpredicted in the RANS simulations throughout the domain. As β is a function of multiple variables, it might be the case that numerical or predictive errors are just canceled out.

Another approach is shown in Fig. 4.8 (b), where the defect shape factor $G = (1 - 1/H)/(u_\tau/U_e)$ is plotted against β. Mellor and Gibson (1966) showed a universal relationship between β and G for an equilibrium boundary layer, and the equilibrium curve by them is also plotted in Fig. 4.8 (b). As

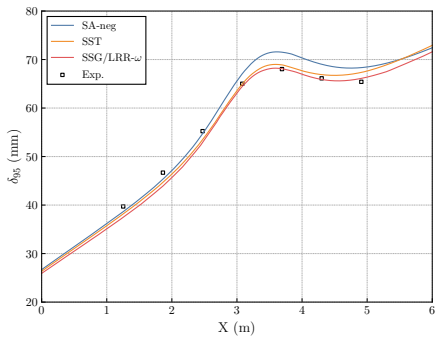

(a) Boundary layer thickness based on 95% edge velocity

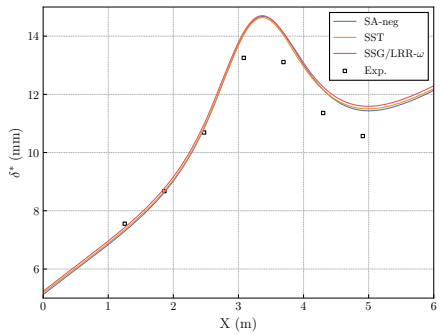

(b) Displacement thickness δ^*

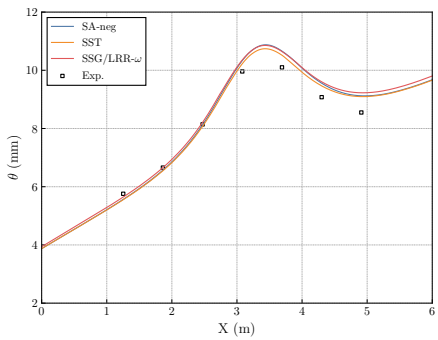

(c) Momentum thickness θ

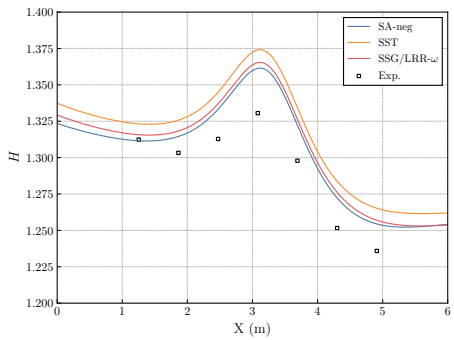

(d) Shape factor H

Fig. 4.7: Different boundary layer thicknesses and the shape factor computed for the 12° case. The experimental results show the rake measurement data at P3 to P9.

expected, the experimental data at the first two stations (P3 and P4) are close to this equilibrium curve, as in this region, the pressure gradient effects (local and non-local) are still small. At the third station P5 and the fourth P6 ($\beta \approx 0.5$), the deviation from the curve seems to be enhanced due to the adverse pressure gradient. At station P7, probably the highest deviation from the equilibrium curve can be observed. Interestingly, at the last station P9, the experimental data point comes back to the vicinity of the equilibrium curve. This might suggest that the flow is returning towards the equilibrium state, relaxing the upstream historical effects.

The model dependency in Fig. 4.8 (b) is relatively small, though it is larger than Fig. 4.8 (a). However, the disagreement between the experimental results and the RANS simulations is more noticeable. The RANS curves appear to be somewhat shifted from the experimental data, although it is very unclear. For example, the transition from the third data point (P5) to the fourth (P6) ($\beta \approx 0.5$) is apparently not captured quantitatively by the RANS curves, but qualitatively, the RANS curves seem to follow the path that the experimental data take. As both G and β are functions of multiple 'lower level' flow parameters, further investigation on each flow parameter might be required to draw any meaningful conclusions.

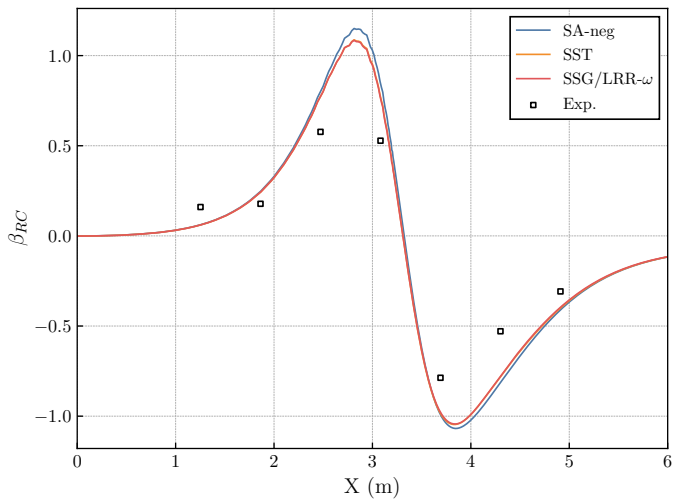

(a) Rotta-Clauser parameter β

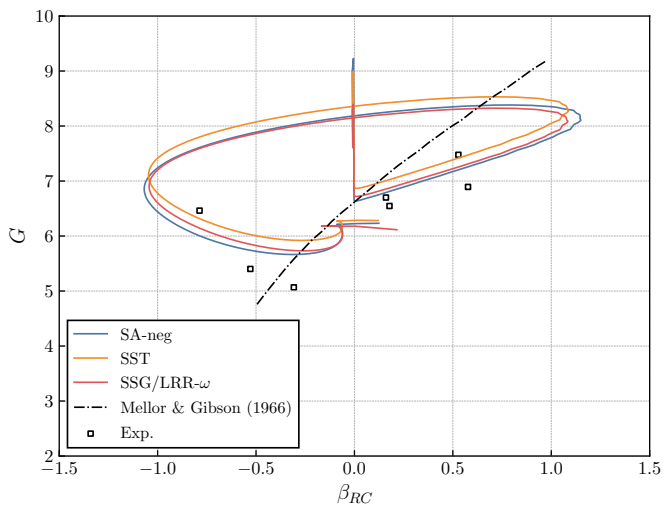

(b) defect shape factor G vs. β

Fig. 4.8: Distribution of Rotta-Clauser parameter β and defect shape factor G vs. β computed for the 12° case. The experimental results show the rake measurement data at P3 to P9.

$-10°$ case

The $-10°$ case shows almost the same tendency as the $12°$ case but in the opposing direction. As shown in Fig. 4.9, C_p is now initially favorable pressure gradient and adverse pressure gradient in the downstream. The skin friction coefficient initially increases due to the acceleration by the favorable pressure gradient, but it turns out to decrease because of the deceleration by the adverse pressure gradient. Similarly to the $12°$ case, the overall underprediction of C_f can be observed. It should be emphasized that both $12°$ case and $-10°$ case underpredict C_f regardless of which pressure gradient comes first. This might support an argument that this discrepancy is mainly affected by things unrelated to pressure gradient effects, such as the accuracy of the rake measurements.

The boundary layer thicknesses (see Fig. 4.10 (a) - (c)) also show similar trends to those of $12°$ case; however, the deviations between the experimental results and the RANS results in the downstream appear to be somewhat smaller in this case. Consequently, the discrepancy between CFD and experiment in the shape factor is also slightly smaller, but the agreement is still not good, especially in the downstream (Fig. 4.10 (d)). The slight predictive improvement of these quantities might be affected by the flow history, i.e., whether the flow initially experiences the adverse pressure gradient or the favorable pressure gradient. However, this is difficult to conclude here due to the other possible source of errors.

Fig. 4.11 (a) shows the distribution of Rotta-Clauser parameter. The opposite direction but similar observations to the $12°$ case can be made. The plot G vs. β is shown in Fig. 4.11 (b). Similarly, the RANS curves only qualitatively capture the departure from the equilibrium curve and its return.

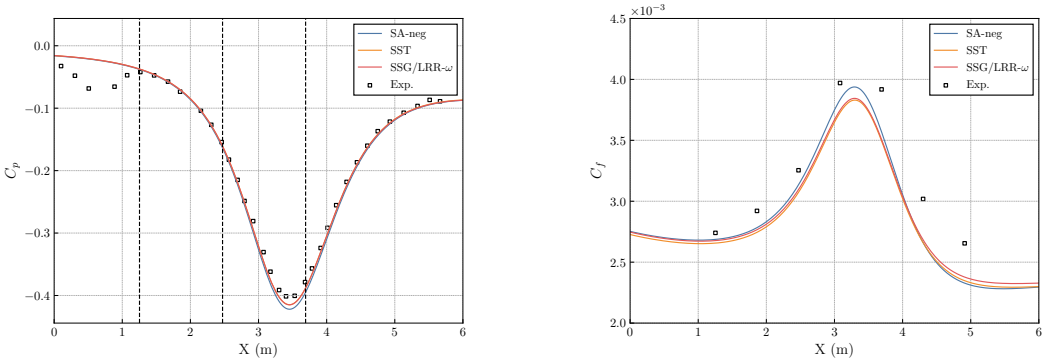

(a) pressure coefficient C_p **(b)** skin friction coefficient C_f

Fig. 4.9: Pressure and skin coefficients computed for the $-10°$ case. The three vertical dashed lines in (a) represent the three rake measurement stations (P3, P5, and P7) where wall profiles are studied in the present work.

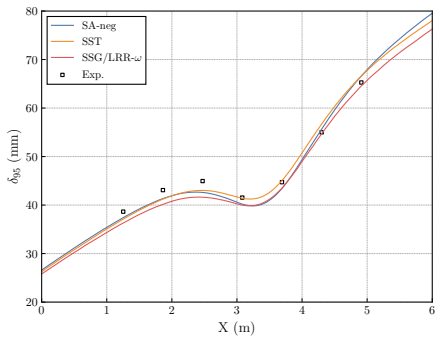

(a) Boundary layer thickness based on 95% edge velocity

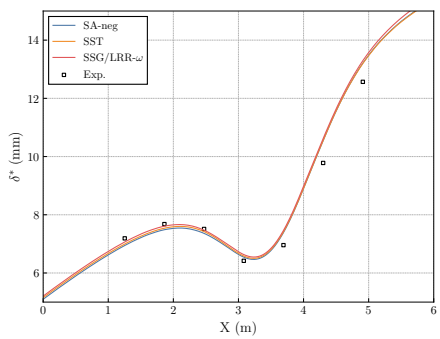

(b) Displacement thickness δ^*

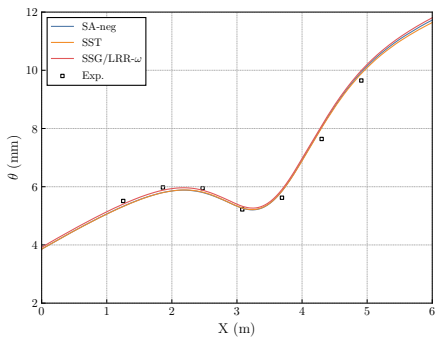

(c) Momentum thickness θ

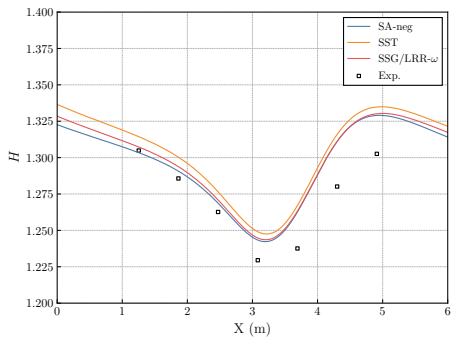

(d) Shape factor H

Fig. 4.10: Different boundary layer thicknesses and the shape factor computed for the $-10°$ case. The experimental results show the rake measurement data at P3 to P9.

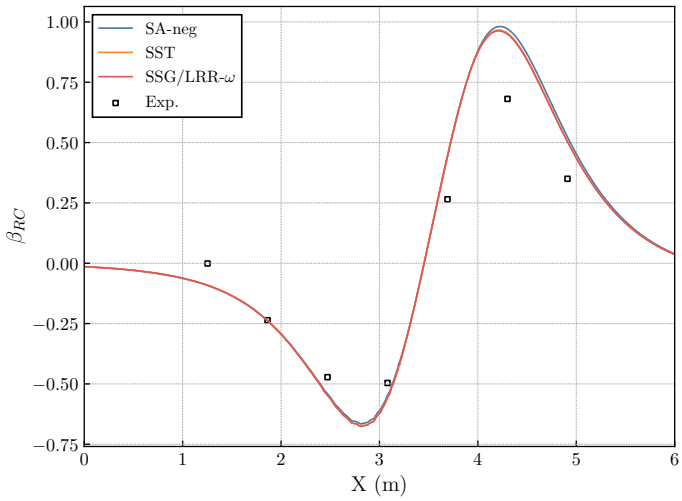

(a) Rotta-Clauser parameter β

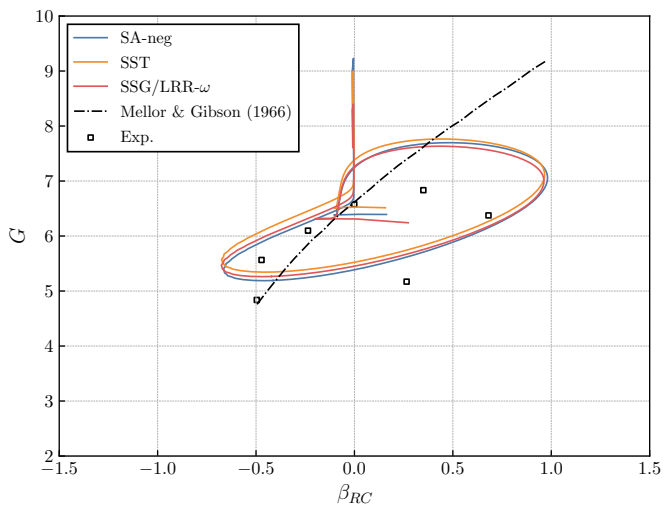

(b) defect shape factor G vs. β

Fig. 4.11: Distribution of Rotta-Clauser parameter β and defect shape factor G vs. β computed for the $-10°$ case. The experimental results show the rake measurement data at P3 to P9.

4.3.2 Wall profiles

For the wall profiles, the three stations are considered in the present work, namely P3 ($x = 1.253\,\mathrm{m}$), P5 ($x = 2.472\,\mathrm{m}$), and P7 ($x = 3.691\,\mathrm{m}$). Each station corresponds to the most upstream measurement plane, the maximum initial pressure gradient, and the maximum secondary pressure gradient, respectively.

12° case

The viscous scaled mean velocity profiles at three stations (P3, P5, and P7) are shown in Fig. 4.12. At the first station P3, where the pressure gradient is still small, albeit non-zero, the agreement between the RANS and the experiment is fairly good from the logarithmic layer to the wake layer. The agreement degrades at the second station P5, where the maximum adverse pressure gradient is present. It appears that all RANS models fail to predict the outer part of the profile. This is probably correlated with the underprediction of C_f. However, it might be the case that the RANS models failed to predict the known APG effect, the shift-up of the wake part that was mentioned in Chapter 2. Because the pressure gradient is fairly small in this test case, it is hard to confirm this argument. This overprediction of the wake part remains further downstream at P7, where the maximum favorable pressure gradient exists. The skin friction C_f is underpredicted at this station too.

Regarding the model-to-model comparison, only the SA model shows different buffer layer behavior than the other two models. The results of Menter SST and SSG/LRR-ω models are overlapping with each other, which could be correlated with the fact that they both are based on the same length scale equation (ω-equation).

The outer scaling of the mean velocity using the edge velocity and δ_{95} is presented in Fig. 4.13. The CFD-to-experiment disagreement in $y/\delta_{95} < 0.4$ is noticeable at P5 and P7, which may correlate with the underprediction of C_f.

-10° case

The viscous scaled mean velocity profiles for the -10° case at three stations (P3, P5, and P7) are presented in Fig. 4.14. Again, the agreement between the RANS and the experiment at P3 is excellent throughout the wall distance. The agreement is still good at the second station P5 where the maximum favorable pressure gradient is present. Also, the known FPG effect, the shift-down of the wake part, can be observed in the experimental result and appear to be also captured in all RANS simulations. At station P7, the appreciable overprediction of the outer part exists. This is again likely due to the underprediction of the C_f at this station.

The mean velocity scaled by the edge velocity against y/δ_{95} is presented in Fig. 4.15. Excellent CFD-to-experiment agreements are observed at P3 and P5, but the misprediction in $y/\delta_{95} < 0.4$ is again observed at P7, similarly to the 12° case.

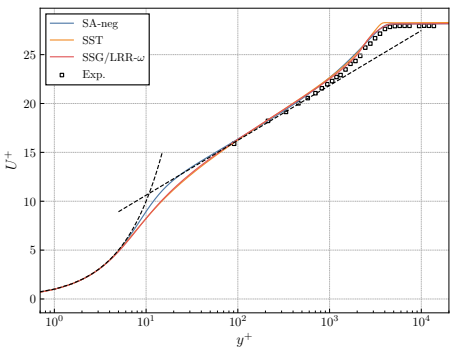

(a) P3

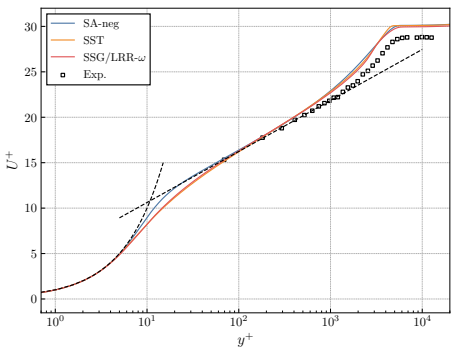

(b) P5

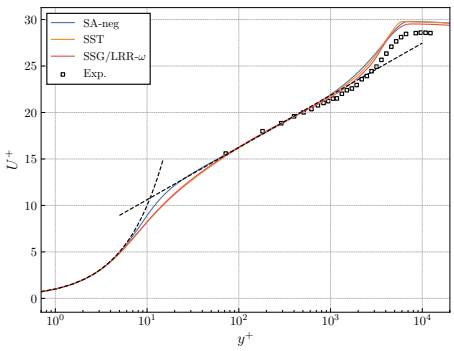

(c) P7

Fig. 4.12: The viscous scaled mean velocity profiles at three stations (P3, P5, and P7) computed for the 12° case. Log-law with $\kappa = 0.41, B = 5.0$ and linear relation in the viscous sublayer are marked with black dashed lines. The experimental results show the rake measurement data.

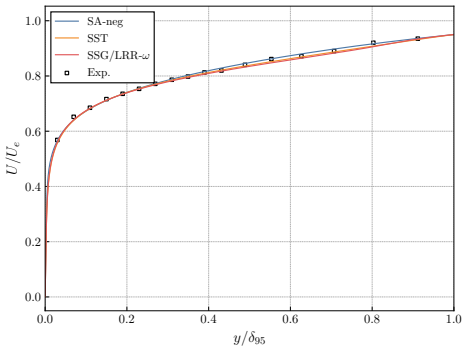

(a) P3

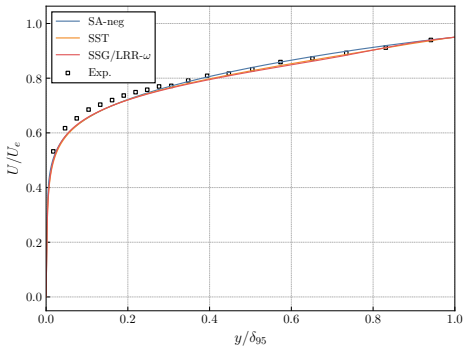

(b) P5

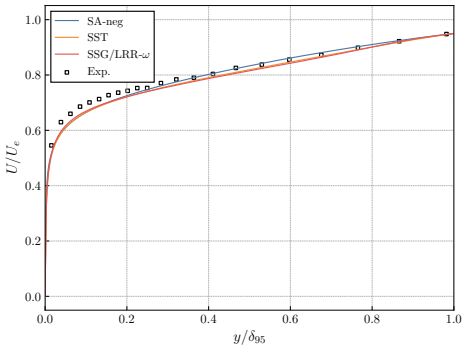

(c) P7

Fig. 4.13: The mean velocity profiles U/U_e vs. y/δ_{95} at three stations (P3, P5 and P7) computed for the 12° case. The experimental results show the rake measurement data.

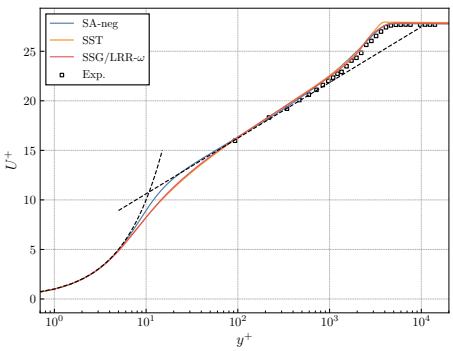

(a) P3

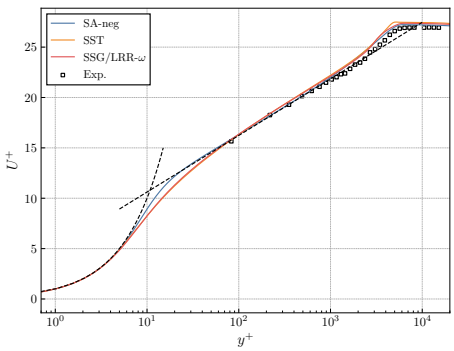

(b) P5

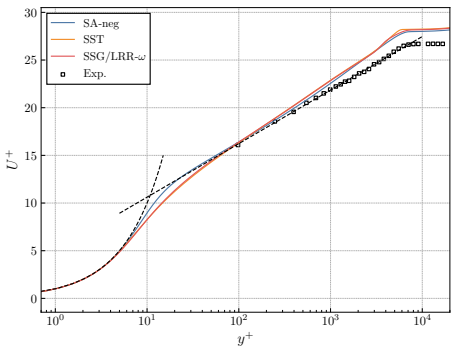

(c) P7

Fig. 4.14: The mean velocity profiles U/U_e vs. y/δ_{95} at three stations (P3, P5 and P7) computed for the $-10°$ case. Log-law with $\kappa = 0.41, B = 5.0$ and linear relation in the viscous sublayer are marked with black dashed lines. The experimental results show the rake measurement data.

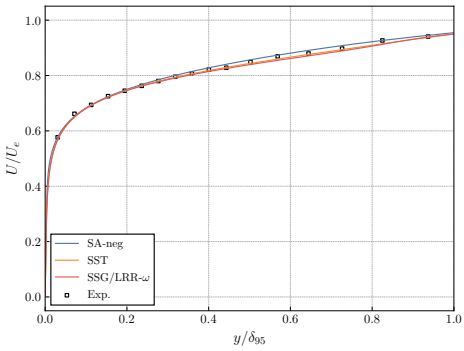

(a) P3

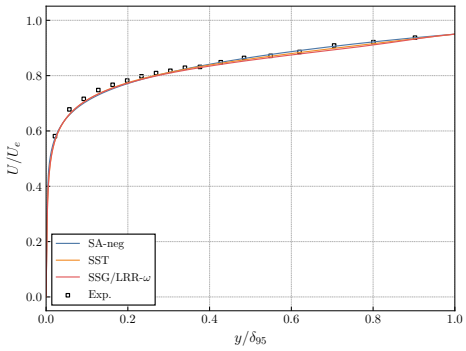

(b) P5

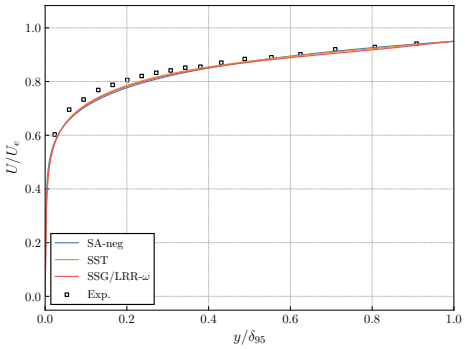

(c) P7

Fig. 4.15: The mean velocity profiles U/U_e vs. y/δ_{95} at three stations (P3, P5 and P7) computed for the $-10°$ case. The experimental results show the rake measurement data.

4.4 Summary

In this chapter, the first test case, the Virginia Tech Stability Wind Tunnel (VTSWT) experiment, was studied. The experimental results were compared with the RANS simulations. Three turbulence models, SA-neg, Menter SST, and SSG/LRR-ω, were compared to investigate each model behavior. Major findings and discussion points are summarized as follows:

- The pressure coefficient evolution and the boundary layer parameters at the first measurement station are successfully replicated by the developed 2D computational set-up.
- Boundary layer thicknesses were overpredicted downstream, while the skin friction coefficient was underpredicted throughout the domain. The reasons are still unclear, and we must wait for more detailed PIV measurements with a higher spatial resolution in the inner part of the boundary layer and 3D computations planned in the future.
- Overall, the RANS model-to-model agreement is fairly good for almost all results. Some exemptions were δ_{95}, H, and the buffer layer of the U^+-profile.
- The existing RANS models are, at least qualitatively, capable of accounting for the non-local, historical effects of the streamwise varying pressure gradients.
- The comparisons between two flow cases might suggest that the change from FPG to APG could be captured in better agreement with the experimental data than the change from APG to FPG.
- The departure of the flow from equilibrium was assessed using the universal relations between the defect shape factor G and β proposed by Mellor and Gibson (1966). The agreement of the RANS results with the experimental data was found to be qualitatively reasonable but showed potential for further improvement.

Chapter 5

LML Wind Tunnel Experiment

This chapter describes the second test case, the Laboratoire de Mécanique de Lille (LML) Wind Tunnel experiment. The experiment was performed in the framework of the EuHIT European project. See Cuvier et al. (2017) for the overview of the experiment. Section 5.1 gives an overview of the experiment and measurement techniques. Section 5.2 describes the computational set-ups including the development of the computational grids and numerical methods. Section 5.3 presents the obtained results and the discussions. Section 5.4 briefly summarizes the main findings on this test case.

5.1 Experimental set-ups

5.1.1 Description of the Experiment

The experiment was conducted in the LML turbulent boundary layer wind tunnel. The test section is 20.6 m long and has a 2 m wide and 1 m high cross-section. The top and bottom walls are perfectly aligned to be parallel. The same holds for the side walls. All sides of the test section are transparent, allowing full optical access. In the EuHIT experiment, a specially designed ramp geometry was installed on the bottom surface of the wall in order to generate pressure gradients. The boundary layer trip is equipped at the tunnel entrance. Fig. 5.1 shows the test section of the LML wind tunnel with the ramp model.

The CAD views of the ramp geometry is illustrated in Fig. 5.2, and the sketch of the ramp geometry is shown in Fig. 5.3. The ramp model consists of three parts. The first part is a contraction part with a length of 1330 mm. The contraction part is followed by a flat plate with $+1.5°$ inclination angle and a length of 2140 mm. This flat plate creates an approximately constant favorable pressure gradient regime. We refer to this flat plate as an FPG flat plate hereafter. The FPG plate is followed by another longer flat plate at $-5°$ inclined angle and 3470 mm length. This creates an approximately constant adverse pressure gradient region, and similarly, we refer to this plate as an APG flat plate in the following. The leading edge of the model was located 9.4 m downstream from the test section entrance.

Fig. 5.1: The LML boundary layer wind tunnel with the ramp model (Cuvier et al. (2017))

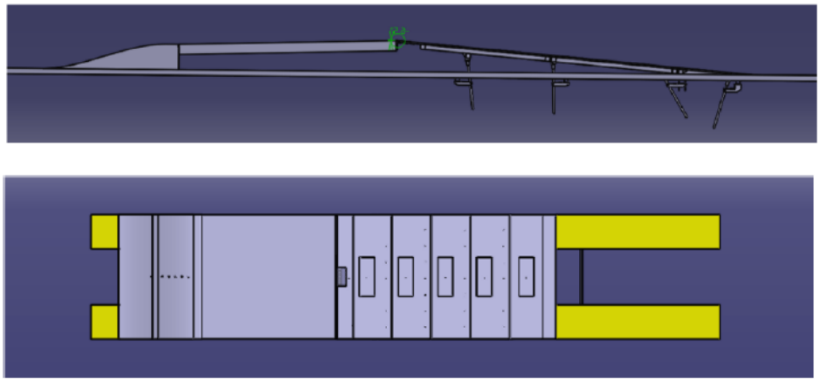

Fig. 5.2: The CAD geometry of the ramp model (Cuvier et al. (2017))

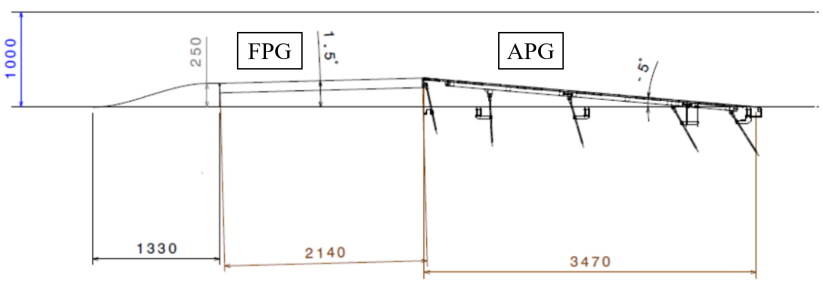

Fig. 5.3: The illustration of the ramp geometry (Cuvier et al. (2017))

In the EuHIT experiment, two different Reynolds number cases were investigated: the freestream velocity $U_\infty = 5\,\mathrm{m/s}$ and $9\,\mathrm{m/s}$. The freestream velocity was controlled at 10 cm downstream of test section entrance with uncertainty ± 0.5 %. In this thesis, we only focus on the higher Reynolds number case, $U_\infty = 9\,\mathrm{m/s}$.

Coordinate systems

For the sake of better communications, two different coordinate systems will be used in the following. The first one is a global coordinate system $x - y - z$; x starts from the test section entrance, y begins at the bottom wall of the wind tunnel, and $z = 0$ corresponds to the mid-plane of the test section. The second coordinate system is a local curvilinear coordinate system s whose origin is located at the leading edge of the ramp geometry. The coordinate s is defined along the surface of the ramp. The sketch of these coordinate systems is shown in Fig. 5.4.

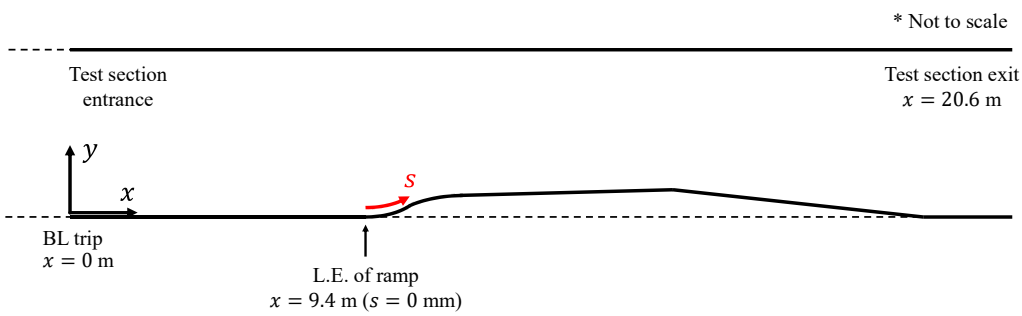

Fig. 5.4: The global and local coordinate systems. The global coordinate x starts at the test section entrance, and y at the bottom wall. The curvilinear coordinate s starts from the leading edge of the ramp model and is along the surface of the ramp.

5.1.2 Measurement Technique

Different PIV measurement techniques were used in the experiment depending on the region of interest. The test section was globally seeded using an evaporated-recondensed water-glycol mixture for all PIV measurements. The diameter of the aerosol particle was approximately 1 μm. In the following, each measurement set-up will be briefly described. Further details can be found in Cuvier et al. (2017).

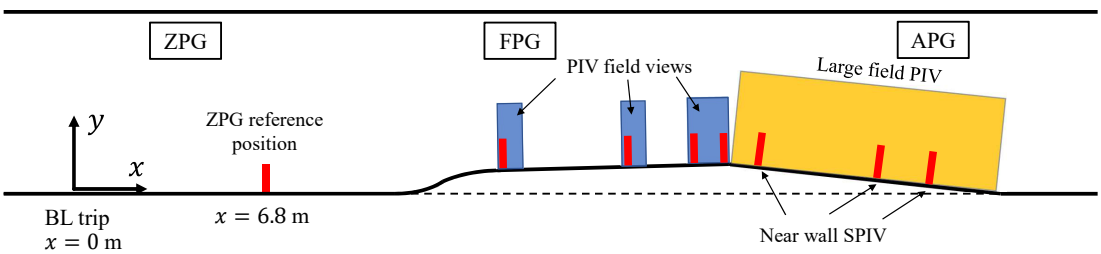

Fig. 5.5: The sketch of the experimental set-ups and PIV measurement positions. The marks in red represent the stations which will be considered in the following Results section.

PIV in the inflow ZPG region

In the zero pressure gradient (ZPG) region in front of the ramp geometry, PIV measurements were conducted at 6.8 m downstream of the test section entrance (see Fig. 5.5). We refer to this position as the inflow ZPG reference position. Two different PIV measurements were carried out to capture the full profiles of the boundary layer at this station. A time-resolved high magnification 2D2C PIV measurement was conducted to obtain the near-wall flow statistics. The measurement area of 5 mm wide was illuminated by a pair of wave lasers (Kvant Laser, SK). The illuminated images were taken using a high-speed CMOS camera (PCO, Dimax-S4) with a 300 mm telephoto lens (Zeiss 300mm/f2.8). The acquired images were processed using a conventional 2-C PIV processing algorithm (PIVview 3.6, PIVTEC GmbH). The size of the final interrogation window was chosen as 64x8 or 32x8, depending on the particle concentration. In addition, a stereo-PIV (SPIV) measurement was carried out to capture the outer profiles off the wall. A double pulse Innolas laser was used to illuminate the measurement area, and the field of view was taken by two Hamamatsu 2k by 2k cameras with Nikon 105mm lenses (f/8).

Another near-wall PIV measurement data is also available at $x = 3.2\,\mathrm{m}$, but this is not considered in the present work due to the lack of outer profiles of the boundary layer.

PIV in the APG region

The adverse pressure gradient (APG) region was characterized by two different PIV measurement set-ups. The first one is a large field 2D2C PIV measurement with 16 sCMOS cameras, which provides the full field of view (3500 mm long $\times$ 250 mm in height) all along the APG plate. The illumination of the entire domain was made possible using the LML BMI YAG laser system installed on the side of the wind tunnel at $x = 11.6\,\mathrm{m}$ and a set of mirrors. Each camera captures a field of view of 230 mm long $\times$ 273 mm in height, with an overlap region of $10 - 20$ mm. A macro planar 100 mm Zeiss lens was used for all cameras except for three. The three cameras were located close to the wind tunnel pillows, and therefore different lenses were used to avoid the shadows. A camera number 6 and 13 used an 85 mm Zeiss lens, and camera 14 used a 50 mm Zeiss lens (Camera number 1 is the one in the most upstream). The f-values for all cameras except camera 6, 15, and 16 were set to 4. The f-values for camera 6, 15, and 16 were 2.8, 4.8, and 4.8, respectively. The images were processed by a modified version of the Matpiv toolbox by LML.

PIV in the FPG region

The favorable pressure gradient (FPG) region was characterized through 2D2C PIV measurements. The experiment was carried out in two steps with two scientific-CMOS cameras. The first step targeted the area near the end of the FPG plate (the third area highlighted in blue in Fig. 5.5). The two sCMOS cameras with Nikon 105 mm lenses (f/5.6) capture a field of view of 46.5 cm long $\times$ 19.8 cm high. The targeted area was illuminated in the same manner as a large field PIV measurements in the adverse pressure gradient region. In the second step, one sCMOS camera targeted the beginning of the FPG plate (the first area highlighted in blue in Fig. 5.5) with a 23.6 cm long $\times$ 19.5 cm high field of view. The other sCMOS camera's field of view started 4 cm upstream of the middle of the FPF plate with

the same 23.6 cm long × 19.5 cm high area. These targeted areas were again illuminated in the same way as the large field PIV in the APG region. The images were processed by a modified version of the Matpiv toolbox by LML. The initial interrogation windows size was 64 by 64 pixels, and the final window size was determined as 24 by 24 pixels.

Pressure measurement

The pressure distribution on the ramp model was measured using scannivalves and a Furness FCO 14 manometer. The uncertainty of the reading is ±0.5 %. The ramp model is equipped with 27 pressure taps in the streamwise direction and 24 for four transverse stations (two on the FPG plate and the other two on the APG plate). The tap number 17, which showed the smallest pressure, was chosen as a reference position for the pressure coefficient. Thus, a pressure coefficient C_p is computed as in Eq. (5.1) with ρ being the density, U_∞ the freestream velocity, P_{17} the static pressure at tap 17. The pressure distribution on the top wall was measured using a plate that had three pressure taps. The plate was moved all along the top wall to obtain the full distribution of the pressure.

$$C_p = \frac{P - P_{17}}{\frac{1}{2}\rho U_\infty^2} \tag{5.1}$$

5.2 Computational set-ups

5.2.1 Computational Grid

The computational grid has been developed using the grid generation software Pointwise. The developed Pointwise grid is illustrated in Fig. 5.6. The grid is 2D and hybrid structured; the structured boundary layer meshes are generated both on the top and bottom wall to resolve the boundary layer profiles, and the area in between is discretized by unstructured meshes. The target y^+ on the first grid point off the wall is around 0.125.

At first, the grid was generated using exactly the same geometry as the wind tunnel test section, i.e., the inlet of the computational domain corresponds to the entrance of the test section. However, this resulted in a significant mismatch of the characteristic boundary layer parameters between CFD computations and the experiment. Thus, the inlet position was slightly elongated through trial and error such that the boundary layer parameters are matched with the experimental results. In the final grid, the displacement thickness δ^*, momentum thickness θ, and friction velocity u_τ are matched within around 3 % differences from the experimental data with the inflow area elongated by 1.2 m. The number of cells in the final mesh is 428,610.

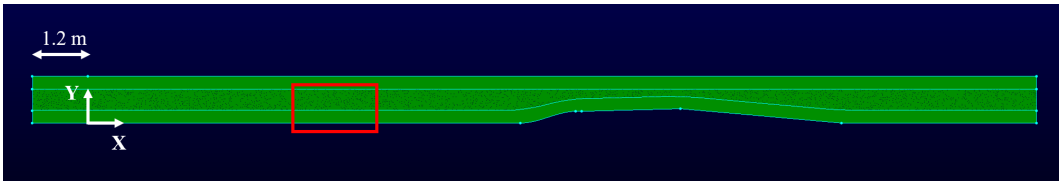

(a) Overview of the computational grid and its coordinate system

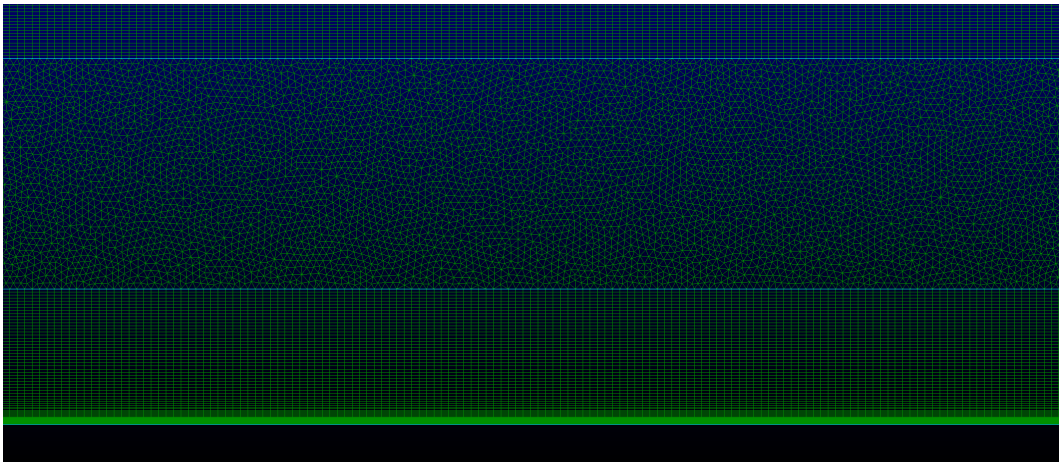

(b) Zoomed image of the grid marked in red in (a)

Fig. 5.6: The developed hybrid computational grid.

U_∞	9.0 m/s
ν	1.5×10^{-5} m^2/s
T_∞	293 K
ρ	1.209 kg/m^3
Re/m	6.0×10^5

Table 5.1: Baseline reference conditions.

5.2.2 Numerical Methods

The numerical simulations were again performed using the DLR-TAU code. The inviscid fluxes of the mean flow are computed by the second-order skew-symmetric Kok central differencing scheme with artificial matrix dissipation. For the turbulence equations, a second-order central scheme is used for one-equation turbulence models, whereas the second-order Roe upwind scheme is applied for two-equation turbulence models and the differential Reynolds stress models. For a temporal discretization, an implicit backward Euler scheme solved with the lower-upper symmetric Gauss-Seidel (LU-SGS) scheme is used. The low-Mach number preconditioning is also applied to improve the solution accuracy using the compressible flow solver. Three different turbulence models, the SA-neg, the Menter SST 2003, and the SSG/LRR-ω Reynolds stress model, are compared.

The boundary conditions used in the numerical simulations are as follows. A non-slip wall boundary is used both on the top and bottom walls. At the inlet of the computational domain, a so-called "reservoir-pressure inflow" boundary condition is applied, where the total pressure and total density are prescribed. At the outlet, a so-called "exit-pressure outflow" boundary condition is used. As described in the previous chapter, TAU prescribes the static reference pressure at this exit by default. However, due to the very low freestream velocity of this test case, this method failed to produce the freestream velocity in the inflow region. Thus, an alternative approach was used to resolve this issue. The TAU has a functionality called "match measured pressure", with which users can prescribe the input reference pressure at a desired position in the computational domain by modifying the exit pressure during the iteration. This functionality was used at 10 cm downstream of the test section entrance, where the experimental freestream velocity was nominally defined. In this way, the desired freestream velocity was obtained in the inflow region.

The baseline reference conditions are summarized in Table 5.1. As described later, a slightly different freestream velocity is considered in one numerical set-up, but the rest uses these conditions listed here.

5.2.3 Different numerical set-ups and modification of the top wall

In the present study, three different numerical set-ups are used and compared. As discussed later in the Results section in more detail, a first attempt using the perfectly horizontal top wall geometry and the freestream velocity $U_\infty = 9.0\,\mathrm{m/s}$ failed to reproduce the edge velocity development, although other boundary layer parameters seem to be predicted quite well. One of the possible causes is that the boundary layers developing on the sidewalls of the wind tunnel are neglected when using a naive 2D computational domain. In the real experiment, those boundary layers on the sidewalls reduce the effective cross-sectional area seen by the flow, resulting in the flow's continuous acceleration.

Set-up	Top wall	U_∞
No. 1	Flat plate	9.0 m/s
No. 2	Flat plate	9.396 m/s
No. 3	Modified geometry	9.0 m/s

Table 5.2: Three different numerical set-ups considered in the present work.

To account for the sidewall effects, the modification of the top wall, which is proposed in Vaquero et al. (2019) is attempted. The idea is that one modifies the top wall of the 2D computational domain such that the potential flow seen by the bottom wall boundary layer remains close between the 3D case and the 2D case. Fig. 5.7 illustrates the concept of this modification. The effective cross-sectional area seen by the flow (shaded in grey in Fig. 5.7) could be described based on the displacement thickness δ^*. If the displacement thicknesses on all sides of the walls are known at each streamwise position, it is possible to compute the effective cross-sectional area. Here, we want to have the same cross-sectional area in the 2D set-up. Thus, assuming the same width of the wind tunnel test section, one can compute the necessary height of the test section, in case δ^* on the top and bottom wall are known.

Since displacement thicknesses are not known in advance, a few assumptions are made in Vaquero et al. (2019). The first assumption is that the displacement thicknesses on the top and bottom walls are unchanged between the 3D and the 2D configuration. The second one is that the displacement thicknesses on the side walls are the same as the one on the top wall in the 3D configuration. Here, one runs a 2D simulation without the top wall modification and obtain the streamwise developments of δ^*_{top2D} and δ^*_{bot2D}. With the above-mentioned two assumptions, the necessary height of the test section at each position x can finally be computed. See their original paper for further details of the mathematical formulations. The obtained modified geometry is shown in Fig. 5.8.

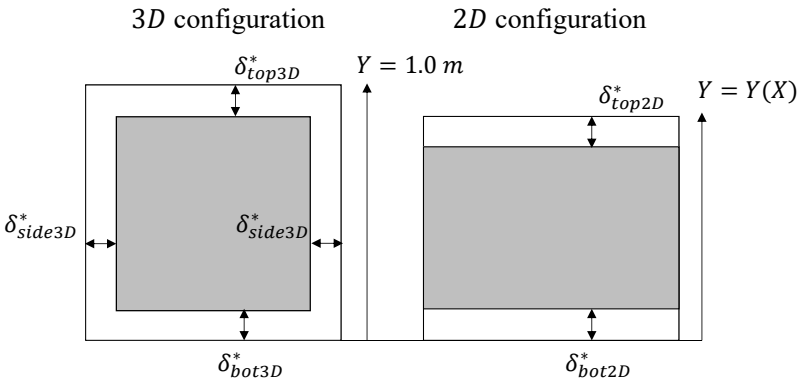

Fig. 5.7: Sketch of the concept of top wall geometry modification proposed by Vaquero et al. (2019).

In addition to the top wall modification, a modification of the freestream velocity is also attempted, such that the edge velocity at the ZPG reference station agrees between the experiment and the CFD simulations. This does not reproduce the additional continuous acceleration due to the sidewall boundary layers. However, this could be an option to consider uncertain effects in the upstream. The three different set-ups are summarized in Table 5.2.

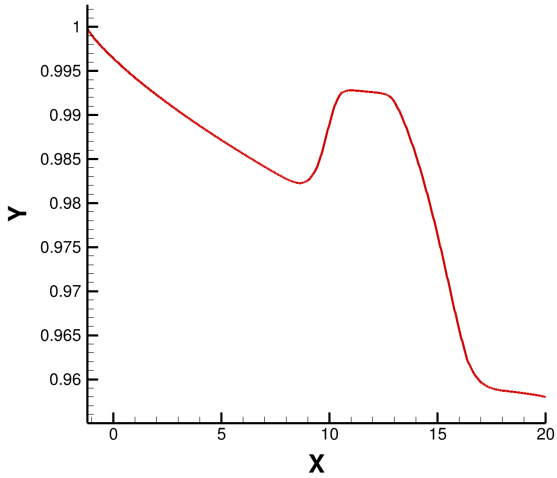

Fig. 5.8: Modified top wall geometry obtained using the SA-neg turbulence model.

5.3 Results

5.3.1 Boundary Layer Parameters

Results from the numerical set-up No. 1

Firstly, we focus on the results obtained with set-up No.1. Fig. 5.9 shows the pressure coefficient C_p on the top and bottom wall. The pressure coefficient on the bottom wall drops sharply around $x = 10$ m due to the contraction part of the ramp geometry. It then jumps up to around 0.5 because of an articulation between the contraction part and the FPG plate. Along the FPG plate, the pressure continuously decreases and runs into another articulation between the FPG plate and the APG plate, which results in a sudden increase of C_p. Then, C_p increases up to around 1.25, traveling along the APG plate.

As can be seen, the turbulence model dependency is almost negligible. This was also observed in the Virginia Tech test case, and this again suggests that the selection of models does not influence the prediction of the freestream behaviors very much.

On the bottom wall, the agreement between the experiment and the RANS simulations is excellent, particularly the agreement in the APG region is surprisingly good. A slight misprediction can be observed in the FPG region. This will be discussed in detail later by comparing the different numerical set-ups. The prediction of the pressure coefficient on the top wall also appears to be good despite an underprediction in the inflow region.

The streamwise development of boundary layer thicknesses is shown in Fig. 5.10 (a)-(c). Similar to the Virginia Tech test case, the model dependency on δ_{99} is fairly high compared to the other two integral boundary layer thicknesses. This is because each turbulence model gives a slightly different dimensional velocity profile from the other. The relatively large variation is no longer noticeable for the integral boundary layer thicknesses δ^* and θ, albeit a slight variation near the end of the domain.

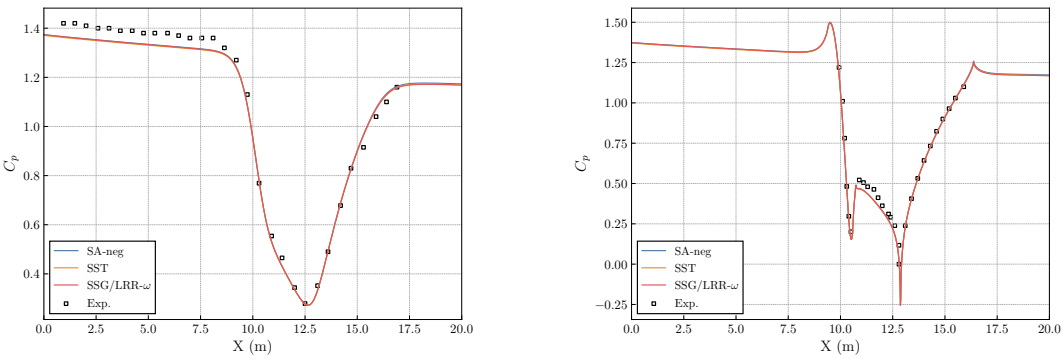

(a) C_p on the top wall **(b)** C_p on the bottom wall

Fig. 5.9: Pressure coefficient C_p on the top and bottom wall obtained with set-up No. 1.

The agreement between the experimental results and the RANS simulations is surprisingly good throughout the domain, especially for δ^* and θ. Two experimental data points near $x = 13$ m correspond to the vicinity of the articulation of the ramp geometry between the FPG plate and the APG plate. Therefore, a slight discrepancy is expected. It should also be pointed out again that there is a good agreement at the ZPG reference position ($x = 6.8$ m) thanks to the manual adjustment of the inflow length of the grid, as discussed in the previous section.

The streamwise development of the shape factor is shown in Fig. 5.10 (d). Despite the excellent agreements in δ^* and θ respectively, the discrepancy between the experiment and the CFD appears to be larger at first glance. However, the order of the mismatch is the same as those of δ^* and θ, which is around $3 - 4$ % at the ZPG reference position.

Fig. 5.11 (a) shows the evolution of skin friction coefficient C_f. All turbulence models are in fairly good agreement with the experimental data, and the variation between the models is small.

Despite the excellent agreements in most boundary layer parameters discussed above, a significant underprediction of the edge velocity is observed in Fig. 5.11 (b). The underprediction is not only on the ramp geometry but also in the inflow region. It appears that all experimental data are somewhat shifted from the RANS curves. Also, as briefly explained in Section 5.2.3, set-up No.1 uses a naive 2D set-up with parallel top and bottom walls, which does not take into account the effects of boundary layers developing on the side walls. In the real experiment, these boundary layers effectively block the flow, and therefore the flow is continuously accelerated. In other words, the flow is accelerated by the additional favorable pressure gradient originating from the sidewall boundary layers.

Apart from the sidewall effects, it might be the case that other influences are one of the primary sources of this discrepancy, such as the inflow conditions. Although the freestream velocity was controlled at $x = 0.1$ m with high accuracy in the experiment, uncertainty still exists about the flow state near the inflow region. For example, the state of the turbulence in the vicinity of the boundary layer trip involves uncertainty in the experiment. Perhaps the boundary layer thickness is hard to determine there. While, in the RANS simulation, the flow is assumed to be fully turbulent throughout the domain, and the boundary layer thickness at the inlet is computed as zero in any case. In addition, the flow state in the inflow region in the experiment might be affected by the upstream conditions (e.g.,

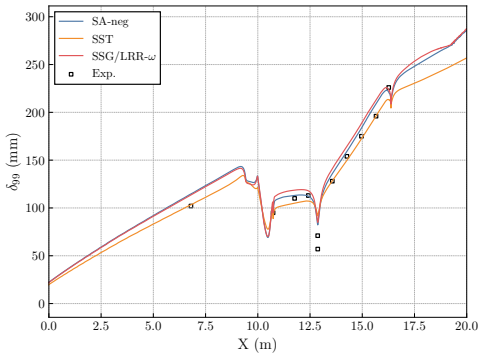

(a) 99 % velocity thickness δ_{99}

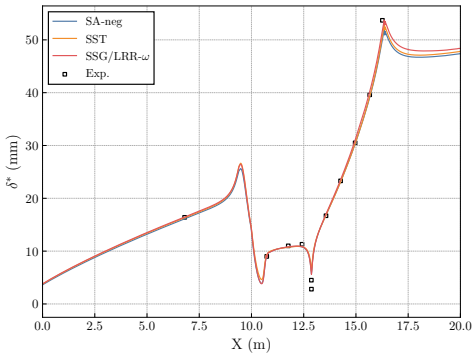

(b) Displacement thickness δ^*

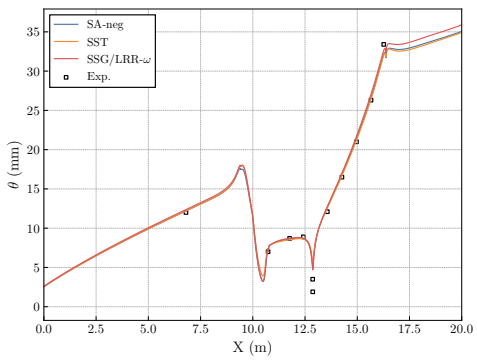

(c) Momentum thickness θ

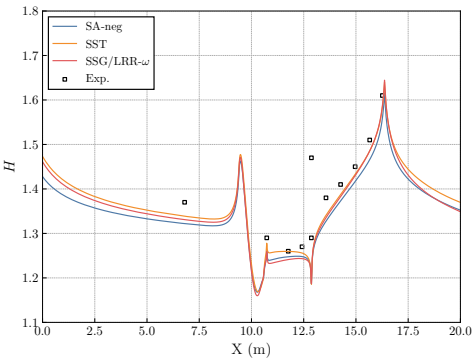

(d) Shape factor H

Fig. 5.10: Different boundary layer thicknesses and the shape factor computed with set-up No. 1.

disturbances from vanes equipped in the chamber, flow state in the contraction section before the test section, etc.) that are not modeled or cannot be modeled in the computational set-ups. These might justify using slightly different freestream conditions in order to match some of the critical parameters.

For those reasons, the present study carried out a sensitivity study comparing three different numerical set-ups as described in Section 5.2.3.

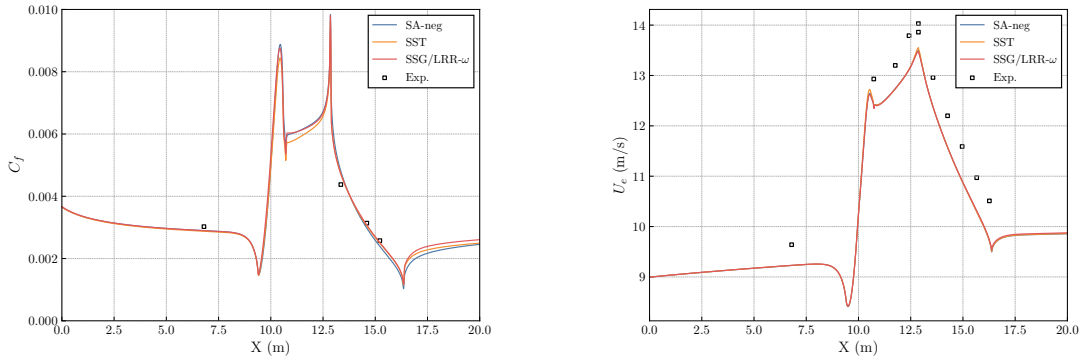

(a) Skin friction coefficient C_f **(b)** Edge velocity U_e

Fig. 5.11: Skin friction coefficient and the edge velocity obtained with set-up No. 1.

Comparison of different numerical set-ups

Fig. 5.12 compares the evolution of the edge velocity obtained with the three different set-ups. The set-up No.2 is calibrated so that U_e matches the experimental data at the ZPG reference position. Yet, the agreement is quite good not only at the ZPG position but also in the FPG and APG region, although it seems that the deviation starts to increase at around $x = 15.0$ m. Set-up No.3, which might be expected to give the best result because it includes the sidewall effects, only results in a minor improvement of the U_e prediction. The acceleration due to the top wall modification is insufficient to reproduce the experimental U_e at the inflow ZPG reference position.

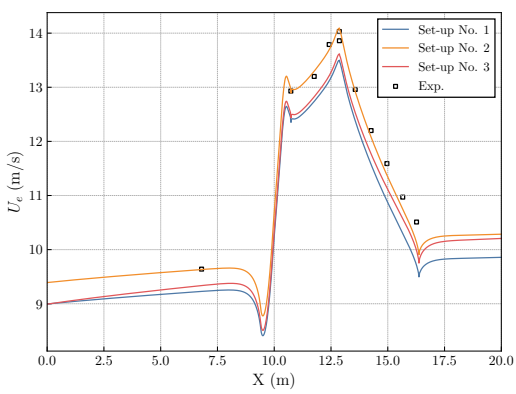

Fig. 5.12: Comparison of the edge velocity between the three different set-ups.

Fig. 5.13 shows the pressure coefficient C_p on the top and bottom wall for three different set-ups. As can be seen in Fig. 5.13 (b), the set-up No.2 with a slightly increased U_∞ shows better agreement in the region. Set-up No.3 also shows a slight improvement in the FPG region. Those suggest that the prediction of the C_p jump at this kink highly depends on the freestream velocity magnitude. Despite the better agreement in the FPG region of set-up No.2, it overpredicts C_p in the APG region. Set-up No.2's overprediction in the APG region is also observed on the top wall. On the other hand, set-up No.3 shows a slight improvement in the prediction of top wall C_p near the inflow region.

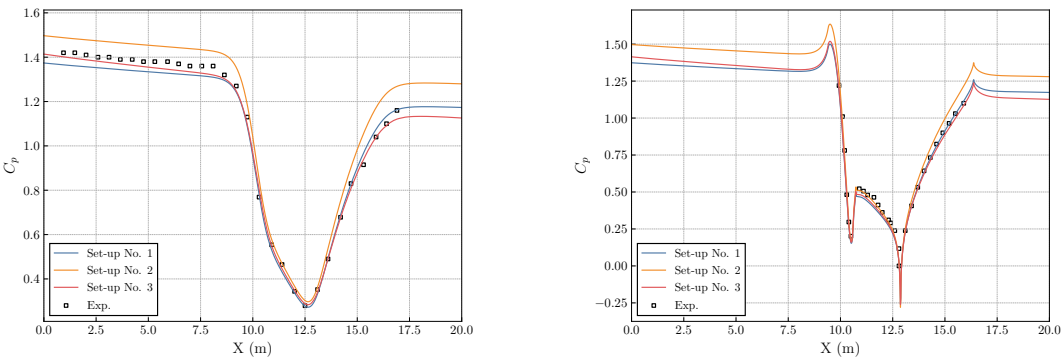

(a) C_p on the top wall **(b)** C_p on the bottom wall

Fig. 5.13: Comparison of pressure coefficients C_p on the top and bottom wall between the three different set-ups.

Fig. 5.14 shows the evolution of δ^* and C_f, whose values are well predicted by the set-up No.1. As can be seen in Fig. 5.14 (a), set-up No.3 shows a worse agreement in the APG region than the other two. The set-up No.2 shows almost the same δ^* as No.1. This might be attributed to the fact that the slight increment of freestream velocity only changes the Reynolds number a little but does not change the flow characteristics very much. On the other hand, the variation in skin friction is relatively small (Fig. 5.14 (b)). Yet, there is a clear difference in the FPG region; only set-up No.2 shows a much higher value. Because no near-wall PIV measurements were carried out in the FPG region, C_f is not available in this region. Further discussion may require determinations of C_f from the available PIV measurement data, which mainly resolves the outer profiles.

Considering the observations mentioned above, one cannot conclude that one of these settings is the best among them. Increasing the freestream velocity (set-up No.2) helps to obtain a better prediction of U_e but gives a worse prediction of bottom wall C_p in the APG region. Taking into account the sidewall effects provides a slight improvement of U_e prediction, but not sufficient. These are important observations and highlight the difficulty of matching all characteristic parameters simultaneously between the experiment and the CFD, using a 2D computational set-up. Other approaches to account for the sidewall boundary layer effects may need to be tested for further studies. Besides, computations using a 3D configuration would also shed light on this discussion.

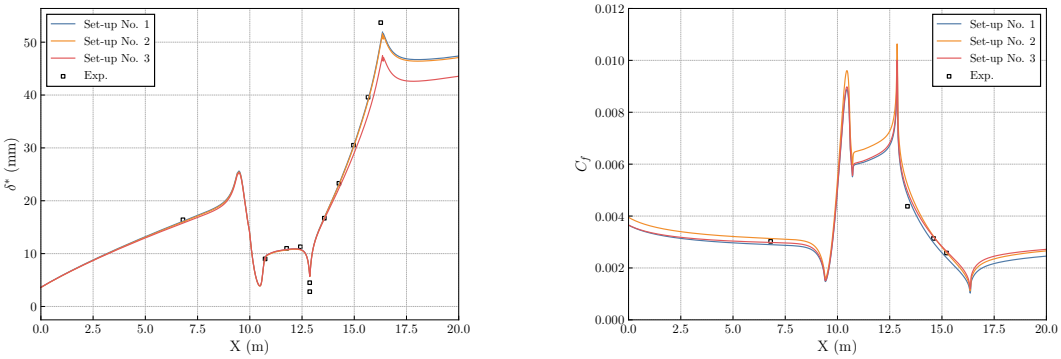

(a) Displacement thickness δ^*

(b) Skin friction coefficient C_f

Fig. 5.14: Comparison of boundary layer parameters between the three different set-ups.

5.3.2 Wall Profiles

In addition to the characteristic boundary layer parameters, wall profiles are also investigated at several stations. Fig. 5.15 illustrates the stations considered in the present study.

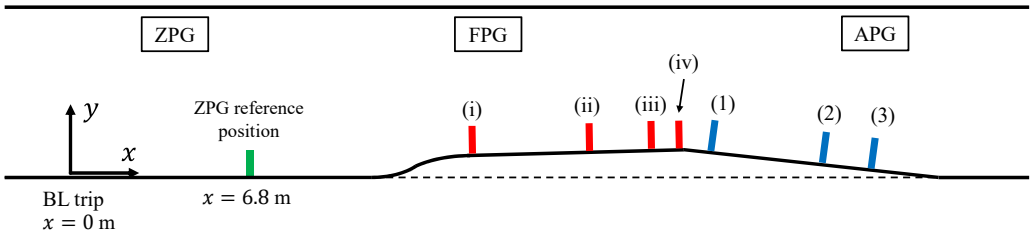

Fig. 5.15: The stations considered in the present work. The stations (i), (ii), (iii), and (iv) in the FPG region are located at $s = 1362\,\text{mm}$, $s = 2392\,\text{mm}$, $s = 3050\,\text{mm}$, and $s = 3497\,\text{mm}$ respectively. The stations (1), (2), and (3) in the APG region are located at $s = 3983\,\text{mm}$, $s = 5233\,\text{mm}$, and $s = 5858\,\text{mm}$ respectively.

Inflow ZPG region

The mean velocity profiles at the ZPG reference station are shown in Fig. 5.16 (a) in viscous scaling. The numerical results are obtained with set-up No.1. The CFD-to-experiment agreement is fairly good except for the underprediction of the wake part. This is most likely due to the underprediction of the edge velocity in set-up No.1. Besides, the classical log-law with $\kappa = 0.41, B = 5.0$ appear to be valid until $y^+ \sim 600$.

The model dependency can only seen between $y^+ \sim 6$ to $y^+ \sim 100$. The Menter SST and SSG/LRR-ω overlap with each other, while the SA-neg shows a higher U^+ in this region. In the logarithmic region, all turbulence models match well with the experimental data.

The turbulent kinetic energy (TKE) profiles at the ZPG reference station are shown in Fig. 5.16 (b) in viscous scaling. The Menter SST and SSG/LRR-ω show almost the same results except for a small difference in the wake part. The RANS and experimental results match well from $y^+ \sim 1000$. The first peak of the TKE in the experimental data is not captured in the RANS simulation because those RANS models do not include a model to capture that.

APG region

Fig. 5.17 shows the viscous scaled mean velocity profiles at three APG stations. The numerical results are again obtained with set-up No.1. First of all, there is a significant discrepancy between the RANS simulations and the experimental results at the first APG station $s = 3.983\,\text{m}$. The classical log-law with $\kappa = 0.41, B = 5.0$ appear to be invalid for the experimental data. It seems that the intercept B is somewhat increased. However, this deviation from the classical log-law no longer exists at the second and third APG stations. The classical log-law seems to be valid until $y^+ \sim 300$ at the last station. This might be explained as follows. The deviation from the classical log-law is introduced by the sudden pressure change between the FPG plate and the APG plate. This could be understood

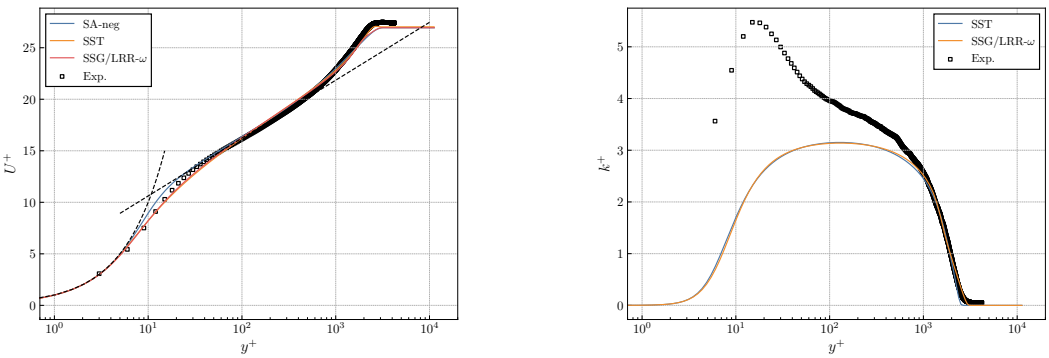

(a) Mean velocity **(b)** TKE

Fig. 5.16: The mean velocity and TKE profiles in wall unit at the inflow ZPG reference station. The results are obtained by computational set-up No. 1. Log-law with $\kappa = 0.41, B = 5.0$ and linear relation in the viscous sublayer are marked with black dashed lines.

as a non-equilibrium effect. Then, the introduced deviation relaxes gradually as the flow travels downstream.

It is also worth discussing that the discrepancy is not only in the log law region but also up until the wake part, where it is even larger. As later shown in Fig. 5.21, the reason for that seems to be not simply because of the underprediction of the edge velocity nor overprediction of the skin friction coefficient, considering the fact that all three set-ups profiles collapse. This CFD-to-experiment mismatch seems to relax in the downstream, and at the second APG station $s = 5.233$ m, the agreement is quite well up until $y^+ \sim 1000$, except the wake part.

As discussed in Knopp et al. (2021), the relaxation of the flow is fast near the wall but much slower in the outer part of the boundary layer. This can be explained by the concept of eddy turnover length and the eddy turnover time. See Sillero et al. (2013) for more details. In this case, the non-equilibrium effect introduced by the rapid transition from the FPG to the APG region may have been relaxed except in the wake part while the flow is traveling from the first APG station to the second APG station. The length of the APG plate $L = 3470$ mm is roughly $\sim 20\delta_{99}$, which might be sufficient for the flow to relax in the wake part but might not be. In principle, the existing RANS models do not explicitly have any mechanism that describes a relaxation of the non-equilibrium effect. Therefore, it is a bit of a surprise that the relaxation in the log-law region appears to be captured by the RANS simulations. However, further investigations of the experimental mean velocity profile are needed to judge the above discussions.

Besides, it is interesting to observe that in Fig. 5.17 (a) the SA-neg still follows the line of the log-law with $\kappa = 0.41, B = 5.0$, while the other two models do not follow this line anymore. A steeper log-law line (i.e., a lower Kármán constant κ) seems to fit these two RANS models results. This appears to hold for the other two stations in the downstream.

Comparing the Menter SST and the SSG/LRR-ω, the difference between these two models is almost negligible for boundary layer parameters and wall profiles, albeit a slight difference in the Reynolds stress prediction as shown later in Fig. 5.18. This accordance is likely due to the same length-scale

equation ($\omega-$equation). Also, it is important to recall that both models are mainly calibrated for equilibrium turbulent boundary layer flows. This result might suggest that even the second-moment closure model is not able to adjust to a non-equilibrium state automatically and requires additional model calibrations and/or improvements for non-equilibrium flows.

Fig. 5.18 shows the Reynolds stress profiles at the three APG stations obtained with the set-up No.1. In general, the RANS results qualitatively match with the experiment for the entire wall distance. A clear difference between the SSG/LRR-ω and the other two models based on Boussinesq's hypothesis can be observed. At the first APG station $s = 3.983$ m, the Reynolds stress is overpredicted by all RANS simulations in the outer part ($y^+ > 700$). This overprediction is less pronounced in the downstream.

Streamwise evolution of the mean velocity

To further investigate the evolution of the mean velocity profile, the FPG region is also studied. Due to the lack of near-wall PIV measurements, the friction velocities at the FPG stations are not available at the moment. For this reason, we only study the dimensional mean velocity profiles in the thesis. For better comparisons between the experiment and the CFD, the results from set-up No.2 are considered here.

Fig. 5.19 shows the mean velocity profiles at four FPG stations. As can be seen, the agreement is quite good near the boundary edge. Interestingly, at the first FPG station $s = 1.362$ m, the experimental data exhibits a hump near $y = 10^{-2}$ m, but this is not captured by the RANS solution. Then, similarly to the discrepancy observed in the APG region, this hump seems to relax as the flow travels downstream. It could be the case that this hump is again introduced by the transition from the contraction part of the ramp to the FPG plate. Since this transition is also from FPG to APG, the same physics might be happening in this region.

Besides that, the mismatch near the wall is presumably due to the poor resolution of the PIV measurements.

Further downstream in the APG region, disagreement from the near wall region up to $y \sim 10^{-2}$ m is observed at the first station. This is less pronounced in the downstream, which corresponds to the mismatch in viscous scaling above discussed.

Comparison of different numerical set-ups

The wall profiles are also compared between three different set-ups. The results are obtained using the SA-neg model.

Fig. 5.21 shows the mean velocity profiles in wall unit at several stations. At the ZPG reference position (Fig. 5.21 (a)), it is interesting to see that the mean velocity profiles of the three different set-ups collapse, especially in the wake part, despite the fact that they have different edge velocities. If we go back to Fig. 5.14 (b), one can see that the highest predicted C_f is obtained by set-up No.2, the second-highest by the set-up No.3, and the lowest by the set-up No.1. Similarly, the edge velocity

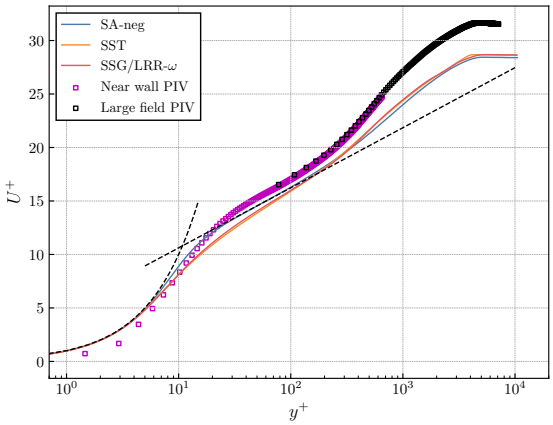

(a) $s = 3.983$ m

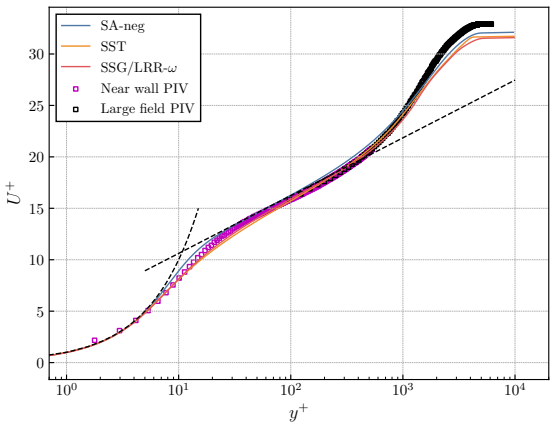

(b) $s = 5.233$ m

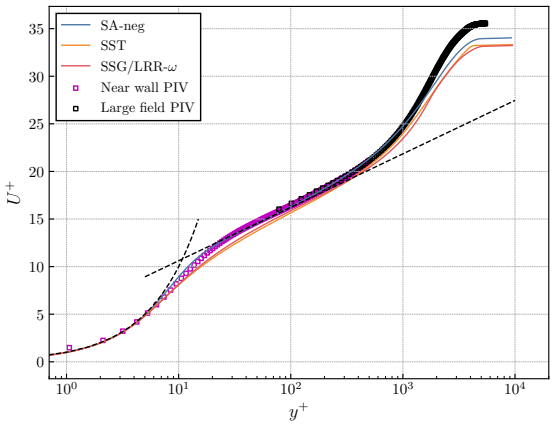

(c) $s = 5.858$ m

Fig. 5.17: The mean velocity profiles in wall unit at three stations in the APG region. The results are obtained by computational set-up No. 1. Log-law with $\kappa = 0.41, B = 5.0$ and linear relation in the viscous sublayer are marked with black dashed lines.

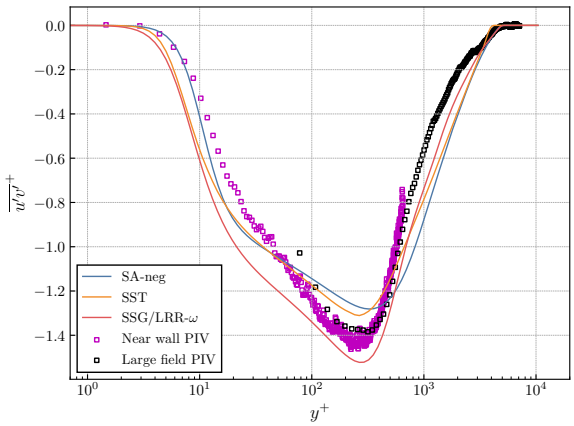

(a) $s = 3.983$ m

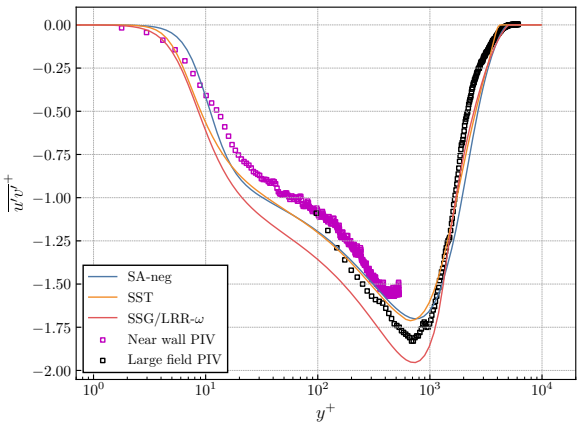

(b) $s = 5.233$ m

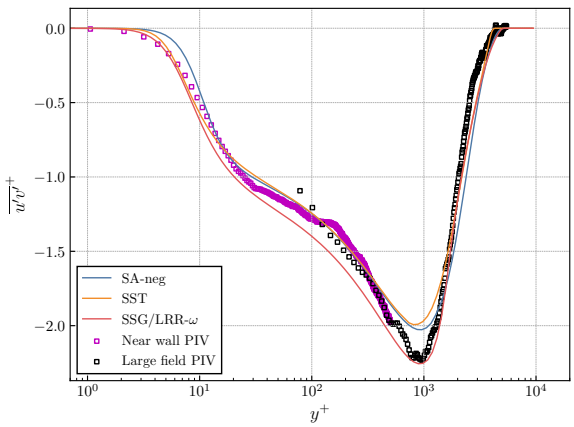

(c) $s = 5.858$ m

Fig. 5.18: The Reynolds stress profiles in wall unit at three stations in the APG region. The results are obtained by the computational set-up No. 1.

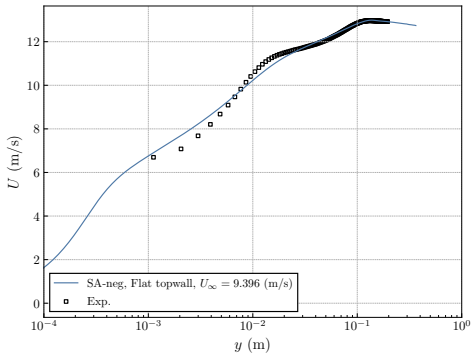

(a) FPG $s = 1362\,\mathrm{m}$

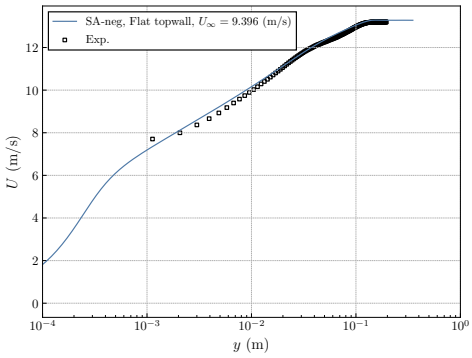

(b) FPG $s = 2.392\,\mathrm{m}$

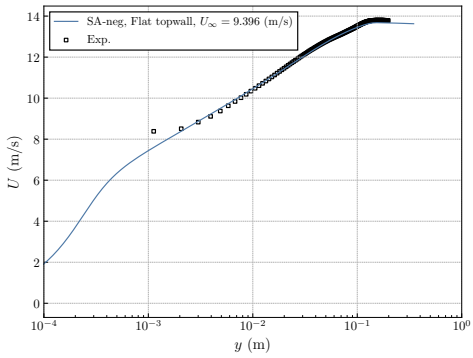

(c) FPG $s = 3.050\,\mathrm{m}$

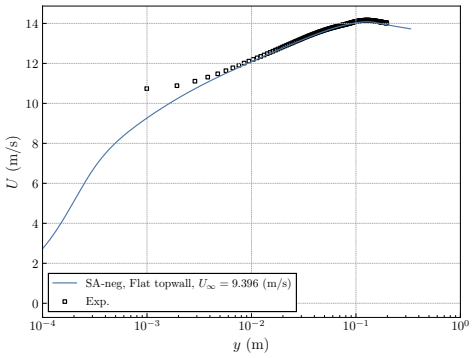

(d) FPG $s = 3.497\,\mathrm{m}$

Fig. 5.19: Dimensional mean velocity profiles at four stations in the FPG region. The results are obtained by the computational set-up No. 2 using the SA-neg.

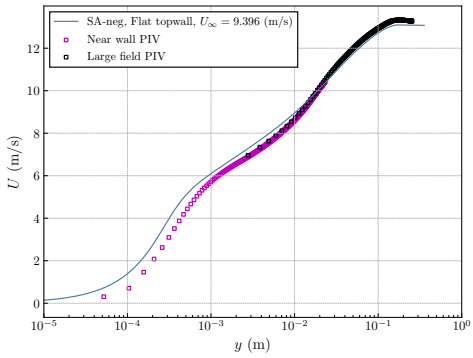

(a) APG $s = 3.983\,\mathrm{m}$

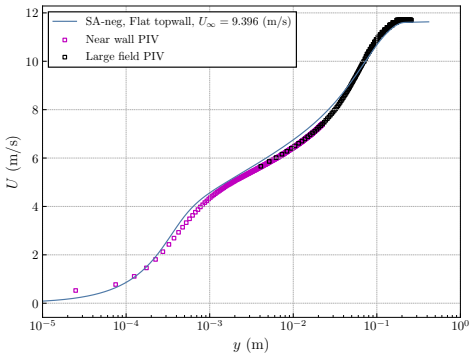

(b) APG $s = 5.233\,\mathrm{m}$

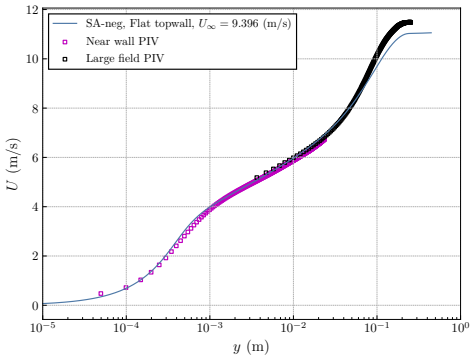

(c) APG $s = 5.858\,\mathrm{m}$

Fig. 5.20: Dimensional mean velocity profiles at three stations in the APG region. The results are obtained by the computational set-up No. 2 using the SA-neg.

is the highest for set-up No.2, the second-highest for set-up No.3, and the lowest for set-up No.1. This explains the collapse of the mean velocity profile in viscous unit for the wake part.

The same observation and explanation can be made for Fig. 5.21 (b), the profile at the first APG station ($s = 3.983$ m). Regardless of whether the computational set-up takes into account the sidewall effects or not, the RANS simulation fails to capture the increment of the wake part of the viscous scaled mean velocity profile due to the APG. This might be an indication that the existing RANS models are incapable of correctly capturing this wake part shift-up due to adverse pressure gradients.

At the last APG station (Fig. 5.21 (c)), set-up No.3 shows a lower wake part than the other two set-ups. The difference between set-up No.3 and the other two is whether the sidewall effects are taken into account or not. As explained earlier, set-up No.3 includes additional acceleration due to the modified geometry, i.e., an additional favorable pressure gradient effect. The shift down of the wake part is likely due to this extra favorable pressure gradient.

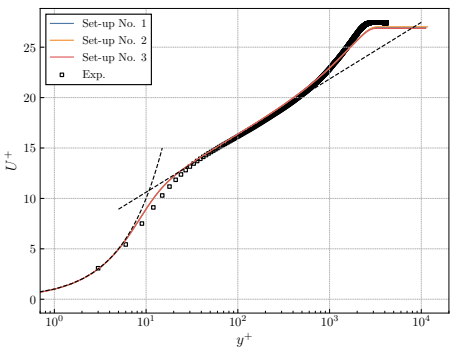

(a) Inflow ZPG reference position

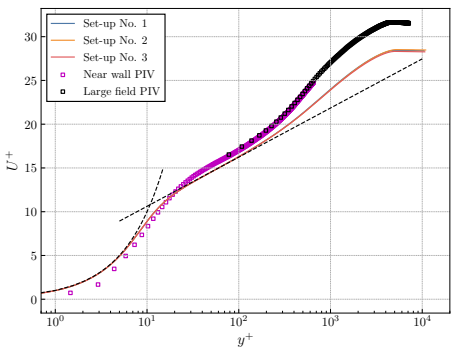

(b) $s = 3.983$ m in APG region

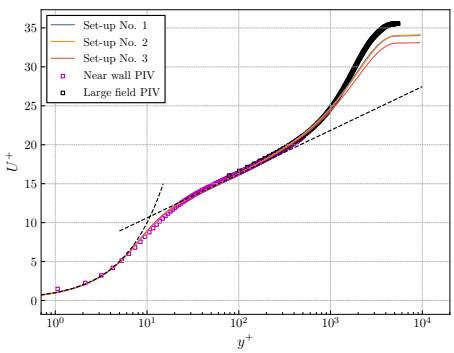

(c) $s = 5.858$ m in APG region

Fig. 5.21: The mean velocity profiles in wall unit obtained with three different set-ups at the ZPG reference station and two stations in the APG region. The results are acquired by using the SA-neg model. Log-law with $\kappa = 0.41, B = 5.0$ and linear relation in the viscous sublayer are marked with black dashed lines.

Finally, the dimensional mean velocity profiles obtained with three different set-ups are also shown in Fig. 5.22.

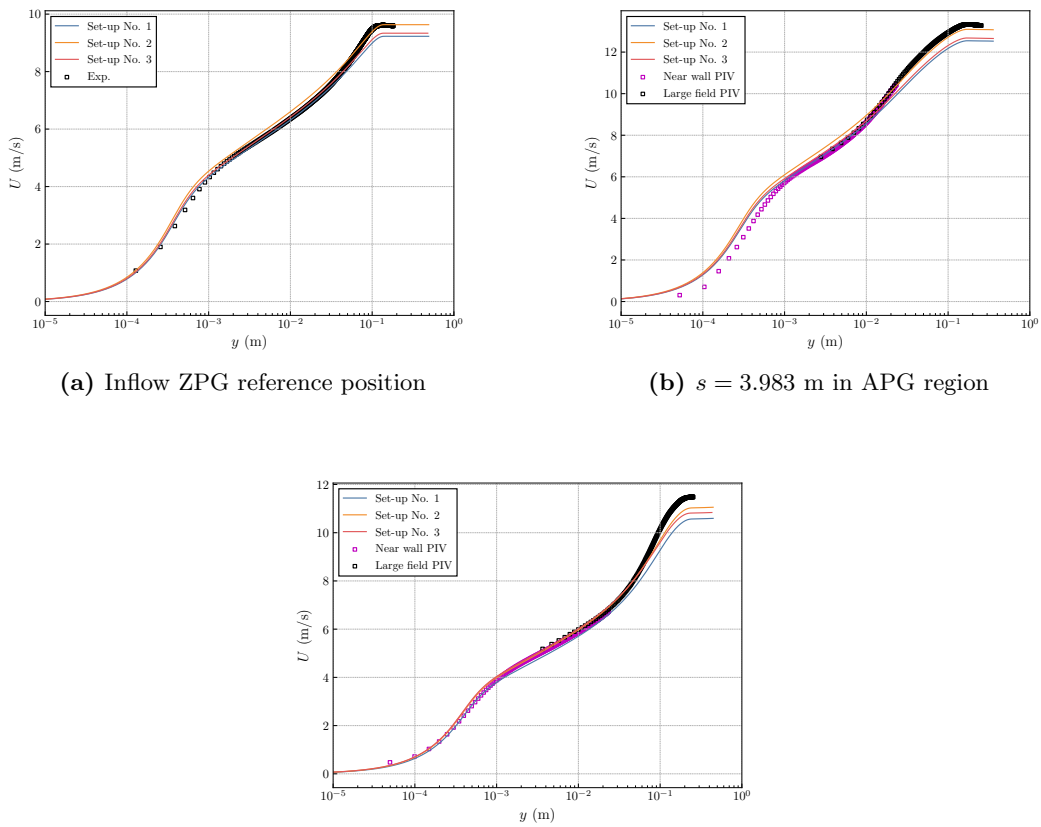

(a) Inflow ZPG reference position

(b) $s = 3.983$ m in APG region

(c) $s = 5.858$ m in APG region

Fig. 5.22: The mean velocity profiles in dimensional unit obtained with three different set-ups at the ZPG reference station and two stations in the APG region. The results are acquired by using the SA-neg model.

5.4 Summary

In this chapter, the second test case, the Laboratoire de Mécanique de Lille (LML) Wind Tunnel experiment was investigated. Firstly, a matching of the characteristic boundary layer parameters was carried out at the inflow ZPG reference station using a naive 2D set-up with a flat top wall (Set-up No.1). Also, three turbulence models, SA-neg, Menter SST, and SSG/LRR-ω, were compared to investigate each model behavior. In addition, three different numerical set-ups were compared in order to discuss 3D effects and which are present in the experiment. The main findings of this test case are summarized below:

- A naive 2D set-up with a flat top wall (Set-up No.1) showed good agreements with the experiment in most boundary layer parameters, although the sidewall boundary layers effects were neglected in this set-up. However, it failed to match the dimensional mean velocity profile, namely the edge velocity.
- Turbulence model dependency is quite small in most boundary layer parameters. Yet, the mean velocity profiles in the APG region showed a slight variation between the SA-neg and the other two; a steeper log-law slope was observed for the Menter SST and SSG/LRR-ω, while the SA-neg seems to follow a classical log-law with $\kappa = 0.41, B = 5.0$.
- A sensitivity study using three different numerical set-ups showed that one could not conclude that one of these settings is the best among them. The set-up No.2 with an increased U_∞ showed an improved prediction of the edge velocity but a worse prediction of the pressure coefficient evolution. On the other hand, set-up No.3, which accounts for the sidewall effects, failed to reproduce the edge velocity as set-up No.1, albeit slightly improved. These observations highlight the difficulty of reproducing a 3D experimental set-up in 2D computations. Other approaches to account for the sidewall effects and/or 3D computations may need to be tested.
- On the viscous scaled mean velocity profile, the RANS results showed significant deviations from the experiment at the first APG station. This is most likely due to the non-equilibrium effect introduced by the pressure transition from the FPG to the APG. This might suggest that the existing RANS models, which are calibrated for equilibrium boundary layer flows, fail to capture the non-equilibrium effects instantaneously.
- A shift-up of the wake part due to APG in U^+-profile was qualitatively captured by all turbulence models. However, the underprediction of the wake part exists even at the last APG station. Quantitative discussions would need to wait for further study of the experimental data and an improved computational set-up such as a 3D configuration.
- The viscous scaled Reynolds stress was qualitatively well predicted by all RANS models. Their mispredictions are larger at the first APG station, which correlates with the large discrepancy in U^+-profile.

Chapter 6

Conclusions

6.1 Conclusions

The present thesis aims to 1) provide a validation database of existing RANS models for high Reynolds number flows with history effects due to streamwise changing mild pressure gradients, and 2) assess the predictive accuracy and its uncertainty of each RANS model. For this purpose, two recent wind tunnel experiments with mild pressure gradients were selected, and the two-dimensional computational set-ups for RANS simulations were defined. The first test case is the wind tunnel experiment conducted in the Virginia Tech Stability Wind Tunnel in the framework of the North Atlantic Treaty Organization (NATO) Science & Technology Organization (STO) Air Vehicles Technology (AVT) 349 project on "Non-Equilibrium Turbulent Boundary Layers in High Reynolds Number Flow at Incompressible Conditions". This flow case involves streamwise changing mild pressure gradients (Rotta-Clauser pressure gradient parameter $\beta = (\delta^*/\tau_w)\, dP/dx \sim 1$ at maximum) and two configurations were studied. One is with an initially adverse pressure gradient followed by a favorable pressure gradient, and the other is with an initially favorable pressure gradient followed by an adverse pressure gradient. The second test case is the wind tunnel experiment conducted in the Laboratoire de Mécanique de Lille (LML) wind tunnel in the framework of the EuHIT European project. This flow case has an approximately constant favorable pressure gradient region followed by again an approximately constant adverse pressure gradient region, generated by a ramp model mounted on the bottom wall of the wind tunnel test section. The pressure gradient of this test case is again mild but slightly higher ($\beta \sim 4$ at maximum) than that of the Virginia Tech test case.

For the Virginia Tech test case, the computational set-ups were determined through the discussions within the collaborative subgroup of the larger NATO AVT-349, and computational grids were developed and shared by Virginia Tech. The grids were developed to match the characteristic boundary layer parameters between the CFD and the experiment in the inflow region. Also, the top wall was modeled as an inclined slip-wall to replicate the experimental pressure gradients on the bottom wall. Finally, RANS simulations were performed using three different turbulence models, the SA-neg, the Menter SST, and SSG/LRR-ω model.

For the LML test case, three different numerical set-ups were considered; 1) a naive 2D configuration with a flat top wall and a freestream velocity $U_\infty = 9.0\,\mathrm{m/s}$ as in the real experiment, 2) one with the same flat top wall as the set-up No.1 but with a increased freestream velocity $U_\infty = 9.396\,\mathrm{m/s}$, 3) one with a modified top wall geometry proposed in (Vaquero et al., 2019) and the freestream velocity $U_\infty = 9.0\,\mathrm{m/s}$. Also, the RANS simulations from three different turbulence models, the SA-neg, the Menter SST, and SSG/LRR-ω model were compared.

Through studying two test cases, many findings have been obtained, and many lessons have been learned. In the following, the conclusions on different aspects will be presented separately.

General difficulties for internal flow test cases

In general, the accurate computational set-up for internal flows is much more difficult to achieve than for external aerodynamic flows, which typically use a far-field boundary condition with a sufficiently large computational domain. This is due to a number of uncertainties present in the wind tunnel experiment. Major sources of uncertainties are summarized below:

- *Origin of the boundary layer.* In a wind tunnel experiment, a laminar to turbulent transition is ensured by a boundary layer trip which is typically equipped upstream of or near the test section entrance. however, at the tripping position, the boundary layer thickness is non-zero and unknown since a non-negligible boundary layer comes from the upstream nozzle.
- *Boundary layers on wind tunnel sidewalls.* An experiment nominally designed as two-dimensional along the center plane of the test section does involve three-dimensional effects such as the blockage effect of the sidewall boundary layers. This displacement effect on the side walls accelerates the real wind tunnel flow in the center plane. With 2D simulations of the flow in the central plane, this effect cannot be taken into account. This sidewall effect becomes even more prominent for strong APG and separation flows. Three-dimensional simulations would be indispensable for such flows.
- *Non-canonical flow conditions at a reference position.* Depending on the experimental configuration, a flow state at an inflow reference position may be non-canonical. For instance, the inflow might contain historical effects before entering the test section. Therefore, matching all characteristic parameters is often arduous and needs to be compromised.
- *Non-unique reference flow conditions during the experiment.* In the experiment, each measurement is performed on a different date and time. Thus, each measurement data is taken at slightly different atmospheric conditions. Typically, the Reynolds number is controlled during the experimental campaign. This would result in a certain variation of freestream velocity, temperature, and/or viscosity. Nevertheless, a single representative reference condition must be determined for CFD simulations. Thus, a careful look must be taken when interpreting the results.

Strategy for determining the suitable computational set-up

Due to a number of uncertainties involved with a wind tunnel experiment, a computational set-up must be carefully determined. Numerical simulations also encompass uncertainties and errors. Only a slightly different numerical setting may result in an appreciable different result. Therefore, such uncertainties should also be assessed or quantified.

Some of the strategies taken in the present work helped to better discuss the results. Below important points and suggestions are summarized:

- Using different RANS models and comparing those results provide an idea of model-dependent uncertainties.
- A mesh refinement study is important to reduce the uncertainty from grid discretizations. Besides, a comparison between meshes that use different topologies would also assess the uncertainty from the grid discretizations.
- Comparisons with the results from different CFD solvers are helpful to assess the variations due to code implementations and compressible/incompressible solvers. This was addressed in the AVT-349 collaboration (Fritsch et al. (2022)).
- A sensitivity study comparing different computational set-ups (as addressed in the LML test case) is helpful to differentiate the source of discrepancy between the CFD and experimental results.
- Assessing not only a few but many different parameters (both dimensional and non-dimensional quantities) is important. For instance, only relying on U^+ vs. y^+ might be dangerous because some of the errors could just cancel out each other. Although matching all parameters at the same time is almost impossible, a suitable computational set-up as a compromise can be found, selecting essential parameters.

Wind tunnel experiment intended as a validation test case for CFD

The author thinks that it is worth accounting for the following conclusions and suggestions for designing new experiments as validation test cases in the future:

1. *Inflow reference position.* As mentioned earlier, the flow state near the entrance is associated with great uncertainty. This typically makes it difficult to find a suitable computational set-up. For this reason, it is better to have not only one but a few reference stations in the inflow region. For future wind tunnel experiments intended as CFD validation test cases, measurement data at several inflow reference stations would be highly appreciated by turbulence modelers.
2. *Importance of near-wall measurements.* For CFD-to-experiment comparisons, the information of the wall profiles in the inner part is of great importance. A PIV measurement with a large field of view to measure from the wall to the boundary layer edge typically gives a large measurement error in the inner part due to the poor resolution near the wall. Thus, special care must be taken when comparing such PIV results for e.g., Reynolds stresses. Also, reliable measurement data near the wall are important to compute the accurate skin friction coefficient C_f, whose value

directly influences the viscous scaled profiles and the pressure gradient parameter β, among others. The Clauser chart analysis is commonly used for computing C_f only from the data in the log-law region. However, only with a few data points, the reliability of the obtained C_f is questionable. Poor estimation of C_f might lead to wrong interpretations of the viscous scaled profile results and pressure gradient effects. Thus, it is important to obtain C_f from a direct measurement technique. In the LML experiment, C_f were determined from the near-wall PIV measurements with high-accuracy (Willert (2015)). A oil film interferometry would also be a great candidate of an alternative method, particularly for flows at very high Reynolds numbers (see Thibault and Poitras (2017) for an overview).

3. *Measurement stations.* A large number of measurement stations along the streamwise direction would be helpful for the turbulence modelers to get a full picture of the flow evolution. This would become more important for studying the flow relaxations, for which a progressive change of the flow needs to be investigated. Therein, near-wall measurements would be highly appreciated by modelers.

Investigation of experimental data

The main findings from the investigation of the experimental data are summarized below:

- *High accuracy demands on the experimental data for validation test cases.* For both test cases with only mild pressure gradients, the changes of the mean velocity profile compared to the standard law-of-the-wall/law-of-the-wake were found to be small. Hence, high accuracy of the measurements is needed to ensure that the uncertainties in the measurements are significantly smaller than the changes of the law-of-the-wall/law-of-the-wake. From this, high accuracy demands on the friction velocity arise. Moreover, the need for a direct method for the friction velocity became obvious, at least in regions of a strong non-equilibrium.
- *Breakdown from the standard logarithmic law.* A breakdown of the universal log-law in the mean velocity could be found in some situations. This was true specifically for the measurement positions in non-equilibrium of the LML experiment.

Predictive accuracy of RANS models for pressure gradient flows with history effects

The present thesis assessed the predictive accuracy of the RANS models for two test cases. Both test cases have streamwise changing pressure gradients and contain history effects, i.e., ZPG $\rightarrow$ FPG $\rightarrow$ APG as in the LML test case. The transition from one to another introduces the non-equilibrium effects into the flow. The major findings through two test cases are summarized below:

- The experiment-to-CFD agreements were good in regions where the flow is in near equilibrium. Some appreciable discrepancies were observed in the region where the flow is at APG and in non-equilibrium. However, the deviations were relatively small due to mild pressure gradients, which is a further reason to demand highly accurate measurement data.

- Overall, the RANS models were found to be, at least qualitatively and in parts quantitatively, capable of accounting for the effects of streamwise varying pressure gradients. For example, the known APG effect, the shift-up of the wake part in U^+-profile, was qualitatively captured by all turbulence models in the LML test case. However, the height of the wake was not quantitatively well predicted. Quantitative discussions would need to wait for further study of the experimental data and an improved computational set-up such as a 3D configuration.
- In the LML test case, the significant underprediction of the viscous scaled mean velocity profile at the first APG station was observed. This is most likely due to the non-equilibrium effect introduced by the pressure transition from the FPG to the APG. This might suggest that the existing RANS models, which are calibrated for equilibrium boundary layer flows, fail to capture the non-equilibrium effects instantaneously. In addition, a greater discrepancy was observed in the LML test case. This is most likely due to the larger pressure gradient coefficient β.
- Overall, turbulence model-to-model comparison showed fairly good agreements in both test cases on most important boundary layer parameters and wall profiles. The performance difference between the first-moment closure and the second-moment closure models was smaller than might be expected. This is likely because the SSG/LRR-ω model uses the same length-scale equation (i.e., $\omega-$equation) as the Menter SST model, and all models are mainly calibrated for equilibrium turbulent boundary layer flows. This result might suggest that even the second-moment closure model is not able to adjust to a non-equilibrium state automatically and requires additional model calibrations and/or improvements for non-equilibrium flows.

6.2 Recommendations for Future Work

Despite the findings described in the previous section, the present work posed several open questions and revealed room for improvement. The possible directions of the future works are listed below:

1. *Further study of experimental data.* The present thesis mainly focused on CFD-to-experiment comparisons and model comparisons. Some discussions did not go beyond qualitative discussions. Although the experimental data were compared with a classical logarithmic law, further study on the experimental data would be needed for quantitative discussions. To name a few examples, 1) quantifications of the wake factor in U^+-profiles, 2) testing other log-law constants and/or checking the existence of a sqrt-law region, 3) comparisons with other experimental pressure gradient flows in the literature.
2. *Testing other 2D set-ups.* In the LML test case, none of the three set-ups gave the best results. How to match the inflow boundary layer parameters and take into account the sidewall boundary layer effects may still have room for improvement. Thus, testing other 2D computational set-ups would help further discussions.
3. *3D computations.* The present work only addressed 2D simulations. As discussed, reproducing a 3D experiment in a 2D computational set-up involves many difficulties, and there is no established way for that. Despite other difficulties in a 3D computation, it should shed more light on the CFD-to-experiment comparisons. Possibly, it provides a better idea to take into account

the 3D effects in 2D simulations. Last but not least, more variations among the turbulence models are expected in 3D computations.

Bibliography

N. Afzal. Wake layer in a turbulent boundary layer with pressure gradient: A new approach. In *Fluid Mechanics and Its Applications*, pages 95–118. Springer Netherlands, 1996. doi:10.1007/978-94-009-1728-6_9.

S. R. Allmaras and F. T. Johnson. Modifications and clarifications for the implementation of the spalart-allmaras turbulence model. In *Seventh international conference on computational fluid dynamics (ICCFD7)*, volume 1902. Big Island, HI, 2012.

C. M. Anderson. *Similarity in adverse pressure gradient turbulent flows*. PhD thesis, School of Engineering and Science, Victoria University of Technology, 2011.

B. Baldwin and H. Lomax. Thin-layer approximation and algebraic model for separated turbulentflows. In *16th Aerospace Sciences Meeting*. American Institute of Aeronautics and Astronautics, jan 1978. doi:10.2514/6.1978-257.

A. Bobke, R. Vinuesa, R. Örlü, and P. Schlatter. History effects and near equilibrium in adverse-pressure-gradient turbulent boundary layers. *Journal of Fluid Mechanics*, 820:667–692, may 2017. doi:10.1017/jfm.2017.236.

F. H. Clauser. Turbulent boundary layers in adverse pressure gradients. *Journal of the Aeronautical Sciences*, 21(2):91–108, 1954. doi:10.2514/8.2938.

F. H. Clauser. The turbulent boundary layer. In *Advances in Applied Mechanics*, pages 1–51. Elsevier, 1956. doi:10.1016/s0065-2156(08)70370-3.

G. N. Coleman, C. L. Rumsey, and P. R. Spalart. Numerical study of turbulent separation bubbles with varying pressure gradient and reynolds number. *Journal of Fluid Mechanics*, 847:28–70, may 2018. doi:10.1017/jfm.2018.257.

D. Coles. The law of the wake in the turbulent boundary layer. *Journal of Fluid Mechanics*, 1(2): 191–226, jul 1956. doi:10.1017/s0022112056000135.

D. E. Coles and E. A. Hirst. Computation of turbulent boundary layers. In *1968 AFOSR-IFP-Stanford Conference, CA*. Stanford Univ. Press, 1969.

C. Cuvier, S. Srinath, M. Stanislas, J. M. Foucaut, J. P. Laval, C. J. Kähler, R. Hain, S. Scharnowski, A. Schröder, R. Geisler, J. Agocs, A. Röse, C. Willert, J. Klinner, O. Amili, C. Atkinson, and J. Soria. Extensive characterisation of a high reynolds number decelerating boundary layer using advanced optical metrology. *Journal of Turbulence*, 18(10):929–972, jun 2017. doi:10.1080/14685248.2017.1342827.

B. J. Daly. Transport equations in turbulence. *Physics of Fluids*, 13(11):2634, 1970. doi:10.1063/1.1692845.

S. A. Dixit and O. N. Ramesh. Large-scale structures in turbulent and reverse-transitional sink flow boundary layers. *Journal of Fluid Mechanics*, 649:233–273, apr 2010. doi:10.1017/s0022112009993430.

P. A. Durbin and S. E. Belcher. Scaling of adverse-pressure-gradient turbulent boundary layers. *Journal of Fluid Mechanics*, 238:699–722, may 1992. doi:10.1017/s0022112092001873.

B. Eisfeld. Turbulence modeling for free shear flows. In *AIAA Aviation 2019 Forum*. American Institute of Aeronautics and Astronautics, jun 2019. doi:10.2514/6.2019-2962.

B. Eisfeld, C. Rumsey, and V. Togiti. Verification and validation of a second-moment-closure model. *AIAA Journal*, 54(5):1524–1541, may 2016. doi:10.2514/1.j054718.

D. Fritsch, V. Vishwanathan, J. Duetsch-Patel, A. Gargiulo, K. T. Lowe, and W. J. Devenport. The pressure signature of high reynolds number smooth wall turbulent boundary layers in pressure gradient family. In *AIAA AVIATION 2020 FORUM*. American Institute of Aeronautics and Astronautics, jun 2020. doi:10.2514/6.2020-3066.

D. Fritsch, V. Vishwanathan, C. J. Roy, T. Lowe, W. J. Devenport, Y. Nishi, T. A. Knopp, P. Ströer, A. Krumbein, R. D. Sandberg, C. Lav, R. Bensow, L. Eca, S. L. Toxopeus, M. Kerkvliet, M. Slama, and L. Bordier. Experimental and computational study of 2d smooth wall turbulent boundary layers in pressure gradient. In *AIAA SCITECH 2022 Forum*. American Institute of Aeronautics and Astronautics, jan 2022. doi:10.2514/6.2022-0696.

Z. Harun. *The structure of adverse and favourable pressure gradient turbulent boundary layers*. PhD thesis, Department of Mechanical Engineering, The University of Melbourne, 2012.

M. B. Jones, I. Marusic, and A. E. Perry. Evolution and structure of sink-flow turbulent boundary layers. *Journal of Fluid Mechanics*, 428:1–27, feb 2001. doi:10.1017/s0022112000002597.

W. Jones and B. Launder. The prediction of laminarization with a two-equation model of turbulence. *International Journal of Heat and Mass Transfer*, 15(2):301–314, feb 1972. doi:10.1016/0017-9310(72)90076-2.

T. Knopp. A new wall-law for adverse pressure gradient flows and modification of k-omega type RANS turbulence models. In *54th AIAA Aerospace Sciences Meeting*. American Institute of Aeronautics and Astronautics, jan 2016. doi:10.2514/6.2016-0588.

T. Knopp. Modification of rans turbulence models for pressure induced separation on smooth surfaces using the dlr victoria experiment. In *AVT 44th Panel Business Meeting Week*, November 2019.

T. Knopp, N. Reuther, M. Novara, D. Schanz, E. Schülein, A. Schröder, and C. Kähler. Experimental analysis of the log law at adverse pressure gradient. *Journal of Fluid Mechanics*, 918, may 2021. doi:10.1017/jfm.2021.331.

T. A. Knopp, D. Schanz, M. Novara, W. Lühder, E. Schülein, A. Schröder, A. Parikh, D. McLellan, M. Bross, F. Eich, and C. J. Kähler. Experimental and numerical investigation of turbulent boundary layers with strong pressure gradients. In *AIAA SCITECH 2022 Forum*. American Institute of Aeronautics and Astronautics, jan 2022. doi:10.2514/6.2022-1035.

J. Kok. A high-order low-dispersion symmetry-preserving finite-volume method for compressible flow on curvilinear grids. *Journal of Computational Physics*, 228(18):6811–6832, oct 2009. doi:10.1016/j.jcp.2009.06.015.

B. E. Launder, G. J. Reece, and W. Rodi. Progress in the development of a reynolds-stress turbulence closure. *Journal of Fluid Mechanics*, 68(3):537–566, apr 1975. doi:10.1017/s0022112075001814.

J.-H. Lee and H. J. Sung. Structures in turbulent boundary layers subjected to adverse pressure gradients. *Journal of Fluid Mechanics*, 639:101–131, nov 2009. doi:10.1017/s0022112009990814.

I. Marusic, B. J. McKeon, P. A. Monkewitz, H. M. Nagib, A. J. Smits, and K. R. Sreenivasan. Wall-bounded turbulent flows at high reynolds numbers: Recent advances and key issues. 22(6):065103, jun 2010. doi:10.1063/1.3453711.

I. Marusic, J. P. Monty, M. Hultmark, and A. J. Smits. On the logarithmic region in wall turbulence. *Journal of Fluid Mechanics*, 716, jan 2013. doi:10.1017/jfm.2012.511.

G. L. Mellor and D. M. Gibson. Equilibrium turbulent boundary layers. *Journal of Fluid Mechanics*, 24(2):225–253, feb 1966. doi:10.1017/s0022112066000612.

F. Menter and C. Rumsey. Assessment of two-equation turbulence models for transonic flows. In *Fluid Dynamics Conference*. American Institute of Aeronautics and Astronautics, jun 1994. doi:10.2514/6.1994-2343.

F. Menter, M. Kuntz, and R. Langtry. Ten years of industrial experience with the sst turbulence model. *Heat and Mass Transfer*, 4, 01 2003.

F. R. Menter. Two-equation eddy-viscosity turbulence models for engineering applications. 32(8): 1598–1605, aug 1994. doi:10.2514/3.12149.

J. Monty, Z. Harun, and I. Marusic. A parametric study of adverse pressure gradient turbulent boundary layers. *International Journal of Heat and Fluid Flow*, 32(3):575–585, jun 2011. doi:10.1016/j.ijheatfluidflow.2011.03.004.

Y. Nagano, M. Tagawa, and T. Tsuji. Effects of adverse pressure gradients on mean flows and turbulence statistics in a boundary layer. In *Turbulent Shear Flows 8*, pages 7–21. Springer Berlin Heidelberg, 1993. doi:10.1007/978-3-642-77674-8_2.

A. E. Perry, J. B. Bell, and P. N. Joubert. Velocity and temperature profiles in adverse pressure gradient turbulent boundary layers. *Journal of Fluid Mechanics*, 25(2):299–320, jun 1966. doi:10.1017/s0022112066001666.

L. Prandtl. 7. bericht über untersuchungen zur ausgebildeten turbulenz. *ZAMM - Journal of Applied Mathematics and Mechanics / Zeitschrift für Angewandte Mathematik und Mechanik*, 5(2):136–139, 1925. doi:10.1002/zamm.19250050212.

M. S. Rao and H. A. Hassan. Modeling turbulence in the presence of adverse pressure gradients. *Journal of Aircraft*, 35(3):500–502, may 1998. doi:10.2514/2.2328.

S. Reuß. *A Grid-Adaptive Algebraic Hybrid RANS/LES Method*. PhD thesis, Georg-August-Universität Göttingen, 2015.

P. Roe. Approximate riemann solvers, parameter vectors, and difference schemes. *Journal of Computational Physics*, 43:357–372, 1981. doi:10.1016/0021-9991(81)90128-5.

J. Rotta. Turbulent boundary layers in incompressible flow. 2(1):1–95, jan 1962. doi:10.1016/0376-0421(62)90014-3.

D. Schwamborn, T. Gerhold, and R. Heinrich. The dlr tau-code: Recent applications in research and industry. In P. Wesseling, E. Onate, and J. Periaux, editors, *European Conference on Computational Fluid Dynamics, ECCOMAS CFD 2006*, TU Delft, The Netherlands, 2006.

C. C. Shir. A preliminary numerical study of atmospheric turbulent flows in the idealized planetary boundary layer. *Journal of the Atmospheric Sciences*, 30(7):1327–1339, oct 1973. doi:10.1175/1520-0469(1973)030<1327:apnsoa>2.0.co;2.

J. A. Sillero, J. Jiménez, and R. D. Moser. One-point statistics for turbulent wall-bounded flows at reynolds numbers up to ≈ 2000. *Physics of Fluids*, 25(10):105102, oct 2013. doi:10.1063/1.4823831.

P. E. Skåre and P. åge Krogstad. A turbulent equilibrium boundary layer near separation. *Journal of Fluid Mechanics*, 272:319–348, aug 1994. doi:10.1017/s0022112094004489.

P. Spalart and S. Allmaras. A one-equation turbulence model for aerodynamic flows. American Institute of Aeronautics and Astronautics, jan 1992. doi:10.2514/6.1992-439.

P. R. Spalart and A. Leonard. Direct numerical simulation of equilibrium turbulent boundary layers. In *Turbulent Shear Flows 5*, pages 234–252. Springer Berlin Heidelberg, 1987. doi:10.1007/978-3-642-71435-1_20.

P. R. Spalart and J. H. Watmuff. Experimental and numerical study of a turbulent boundary layer with pressure gradients. 249(-1):337, apr 1993. doi:10.1017/s002211209300120x.

C. G. Speziale, S. Sarkar, and T. B. Gatski. Modelling the pressure–strain correlation of turbulence: an invariant dynamical systems approach. *Journal of Fluid Mechanics*, 227:245–272, jun 1991. doi:10.1017/s0022112091000101.

B. S. Stratford. The prediction of separation of the turbulent boundary layer. *Journal of Fluid Mechanics*, 5(01):1, jan 1959. doi:10.1017/s0022112059000015.

R. Thibault and G. J. Poitras. Uncertainty evaluation of friction velocity measurements by oil-film interferometry. *Journal of Fluids Engineering*, 139(5), mar 2017. doi:10.1115/1.4035461.

A. A. Townsend. *The Structure of Turbulent Shear Flow.* Cambridge University Press, 1956.

A. A. Townsend. Equilibrium layers and wall turbulence. *Journal of Fluid Mechanics*, 11(1):97–120, aug 1961. doi:10.1017/s0022112061000883.

J. Vaquero, N. Renard, and S. Deck. Advanced simulations of turbulent boundary layers under pressure-gradient conditions. *Physics of Fluids*, 31(11):115111, nov 2019. doi:10.1063/1.5126932.

R. J. Volino. Non-equilibrium development in turbulent boundary layers with changing pressure gradients. *Journal of Fluid Mechanics*, 897, jun 2020. doi:10.1017/jfm.2020.319.

D. C. Wilcox. Reassessment of the scale-determining equation for advanced turbulence models. *AIAA Journal*, 26(11):1299–1310, nov 1988. doi:10.2514/3.10041.

C. E. Willert. High-speed particle image velocimetry for the efficient measurement of turbulence statistics. *Experiments in Fluids*, 56(1), jan 2015. doi:10.1007/s00348-014-1892-4.

K. S. Yajnik. Asymptotic theory of turbulent shear flows. *Journal of Fluid Mechanics*, 42(2):411–427, jun 1970. doi:10.1017/s0022112070001350.

J. M. Österlund, A. V. Johansson, and H. M. Nagib. Comment on "a note on the intermediate region in turbulent boundary layers" [phys. fluids12, 2159 (2000)]. *Physics of Fluids*, 12(9):2360–2363, sep 2000. doi:10.1063/1.1287660.